# Sea Breeze Geoengineering to Increase Rainfall over the Arabian Red Sea Coastal Plains

SULEIMAN MOSTAMANDI,[a] EVGENIYA PREDYBAYLO,[a,b] SERGEY OSIPOV,[b] OLGA ZOLINA,[c,d] SERGEY GULEV,[d]
SAGAR PARAJULI,[a] AND GEORGIY STENCHIKOV[a]

[a] *King Abdullah University of Science and Technology, Thuwal, Saudi Arabia*
[b] *Max Planck Institute for Chemistry, Mainz, Germany*
[c] *Laboratoire de Glaciologie et Géophysique de l'Environnement, Grenoble, France*
[d] *P. P. Shirshov Institute of Oceanology, Russian Academy of Sciences, Moscow, Russia*

ABSTRACT: The Red Sea (RS) has a high evaporation rate, exceeding 2 m of water per year. The water vapor is transported from the shorelines by sea breezes as far as 200 km landward. Relative humidity in the vicinity of the RS exceeds 80% in summer. Nevertheless, precipitation is scarce in most of the Arabian RS coastal plain. In this work we use the Weather Research and Forecasting (WRF) regional model to assess how deliberate changes (geoengineering) in the surface albedo or conversion of bare land to wide-leaf forests over a vast coastal plain region affect precipitation over the Arabian RS coast. Our simulations show that geoengineering of land surface characteristics perturbs coastal circulation; alters temperature, moisture, and momentum exchange between the land surface and atmosphere; and changes the breeze intensity, cloud cover, and eventually the amount of precipitation. We find that extended afforestation and increased surface albedo are not effective in triggering rainfall over the RS coastal plains. Conversely, decreasing surface albedo to 0.2, assuming installation of solar panels over the coastal plains, increases surface air temperature by 1–2 K, strengthens horizontal surface temperature differences between sea and land, intensifies breezes, increases water vapor mixing ratio in the boundary layer above 3 km by about 0.5 g kg$^{-1}$, enhances vertical mixing within the planetary boundary layer, and generates 1.5 Gt of extra rainwater, equivalent to the annual consumption of five million people. Thus, this form of regional land surface geoengineering, along with advanced methods of collection and underground storage of freshwater, provides a feasible solution to mitigation of the existing water crisis in the arid coastal regions.

KEYWORDS: Atmosphere, Dynamics, Precipitation, Sea breezes, Albedo, Evaporation

## 1. Introduction

Water is an essential element of life for all living beings: humans, animals, and plants. Water plays a central and critical role in all aspects of human activity. The majority of countries in the Middle East (ME), including the Kingdom of Saudi Arabia (KSA), are in the middle of a water crisis (Hameed et al. 2019). Management of water resources over the Arabian Peninsula (AP) and the entire ME is challenging. Population growth, industries, and agricultural activities over the past century have led to an increase in demand for water supply (Almazroui et al. 2012). Groundwater resources in the ME countries are rapidly depleting (Rodell et al. 2018). It is predicted that the supply of groundwater in the KSA will become exhausted within 13 years (*Saudi Gazette* 2016), as the KSA has one of the highest per capita rates of water consumption in the world at 280–300 t yr$^{-1}$, in 1985–2010 using on average $9.82 \times 10^9$ m$^3$ yr$^{-1}$ of fresh water (Al-Zahrani et al. 2011; Al-Zahrani and Elhag 2003, 48–56).

The main water sources in the KSA are groundwater, surface water (precipitation runoff), treated water, and desalinated seawater from the Red Sea (RS) and Arabian Gulf.

The most commonly used water desalination methods are highly unsustainable, since they consume a lot of fossil fuel energy (Ahmed et al. 2019). The KSA desalinizes about 1 Gt of water per year in 30 water desalination plants using 1.5 million barrels of oil per day, thus producing 25%–30% of all desalinated water in the world. Water treatment facilities also provide 1 Gt of water annually. Despite the fact that desalination and water treatment provide substantial portions of the required water supply, they are energy-intensive processes and cannot entirely meet the annual water demand.

The total water supply from natural renewable freshwater resources in the KSA is about 6 Gt, and it is controlled by available precipitation (Al-Rashed and Sherif 2000). Groundwater and surface water sources are scarce in the KSA, since the majority of the Arabian Peninsula is hot and dry (Köppen 1936) with little to no precipitation (Al-Jerash 1985; Al-Taher 1994). There are no permanent rivers in the KSA since more than 70% of the area is covered by deserts. About 2 Gt of groundwater is pumped out from aquifers that are nearly 1 km below the surface, and this water is more than 9000 years old. The fossil aquifers are not replenishing and will be exhausted soon, as precipitation only recycles groundwater in shallow aquifers in the upper soil layers. The KSA captures about a quarter of available runoff (0.78 Gt of rainwater annually) in 449 artificial water reservoirs (Tarawneh and Chowdhury 2018; Lopez et al. 2014; Ministry of Environment Water and Agriculture 2017).

---

*Corresponding author*: Georgiy Stenchikov, georgiy.stenchikov@kaust.edu.sa

The annual total rainfall shows a decreasing trend in most regions of the KSA. Almazroui et al. (2012) analyzed 27 ground weather stations for the period 1978–2009 and found that in 1995–2009 there is a significant negative trend of the averaged over the KSA rainfall ($-47.8$ mm decade$^{-1}$). Also, they revealed a positive trend of surface air temperature with a rate of 0.6°C decade$^{-1}$. Winter is considered a "wet" season while the precipitation in summer is very low. The only region in the KSA with regular rainfall is the southwest coast, where the orographic precipitation occurs as a result of interaction between sea breeze flow and mountainous terrain, where land elevation exceeds 2 km. The mean annual precipitation in this region reaches 250 mm (Ter Maat et al. 2006) with the maximum in spring (March or April, 50 mm month$^{-1}$) and the minimum (October, 3 mm month$^{-1}$) in fall (Almazroui et al. 2012). Hasanean and Almazroui (2015) and Almazroui et al. (2012) indicated a positive precipitation trend in the southwestern AP, probably due to northward shifting of the intertropical convergence zone (ITCZ) in summer. The mountain range along most of the Arabian Red Sea coast is not as high as in the southern Red Sea. Therefore most of the inhabited coastal plains of the KSA are much drier than its southern part.

The idea of artificially increasing precipitation over the Arabian Peninsula has attracted attention for many years. The United Arab Emirates (UAE) is currently funding research on a rain enhancement program that explores different technical options (Mazroui and Farrah 2017). The feasibility of cloud seeding for precipitation enhancement was studied in Saudi Arabia in 2007–09 (Kucera et al. 2010), but without convincing results. Afforestation is another proven way of improving environmental conditions that has been practiced for a long time in different climatic zones (Shrestha and Lal 2006). Afforestation simultaneously changes both surface albedo and evaporation. Modification of just surface albedo alone can also change local surface air temperature and affect natural precipitation processes. These methods generally affect only a specific region and have mild consequences in the surrounding areas. They can be developed as climate adaptation measures, and we refer to them here as regional (or local-scale) geoengineering. We use this term in contrast to global geoengineering, which has been proposed to counteract the effects of global warming (Shepherd 2009; Fox and Chapman 2011).

One of the most feasible global geoengineering measures, known as solar radiation management (SRM), involves injecting sulfate aerosol precursors such as $SO_2$ into the lower stratosphere, as occurs with strong volcanic eruptions (Crutzen 2006; Fox and Chapman 2011). Robock et al. (2008) showed that injection of 5 Mt of $SO_2$ per year to the lower stratosphere could decrease global temperature by more than 0.5°C. However, global geoengineering may potentially cause adverse regional impacts and worsen environmental conditions in highly populated regions. For example, SRM could dampen monsoon circulation and decrease rainfall in Sahel (Trenberth and Dai 2007; Haywood et al. 2013; Dogar et al. 2017), leading to far-reaching humanitarian crises and rendering the application of such planetary-scale geoengineering technologies hazardous. A considered and strategic application of geoengineering in a few small areas of Earth would be relatively safe and easy to control.

Land-cover changes are the major forcings that, along with greenhouse gases and aerosols, drive regional and global climate change (Vitousek et al. 1997; Feddema et al. 2005; Foley et al. 2005; Cao et al. 2015). Forests play a vital role in local climate regulation due to their interaction with the hydrological cycle. Forests have relatively low surface albedo and absorb more solar radiation than desert land. However, to maintain a favorable thermal regime, trees facilitate evaporation through transpiration, which cools the surface layer and facilitates precipitation. The role of land-use changes in altering convective rainfall has been simulated in (Pielke 2001; Pitman 2003). They demonstrated that landscape changes alter surface energy and moisture budgets, affecting the intensity of deep cumulus convection. The influence of land use on precipitation and latent and sensible heat fluxes was demonstrated in Chen and Avissar (1994a,b). Junkermann et al. (2009) found that large-scale modification of vegetation cover can change local convection and water vapor availability. Pielke et al. (2007) analyzed how the regional landscape affects rainfall. Kunstmann and Jung (2007) used the fifth-generation Pennsylvania State University–National Center for Atmospheric Research Mesoscale Model (MM5) for West Africa to investigate the role of initial soil moisture on total rainfall and on the recycling of precipitation. Precipitation recycling in central Sudan has been studied in (Eltahir 1989; Eltahir and Bras 1996). They showed that the high levels of evaporation from the Bahr Elghazal basin have a significant effect on the climates of neighboring dry regions. Krenke et al. (1991) compared the climate impacts of large-scale surface albedo and soil moisture changes in the scope of the tropical deforestation study. Interestingly, Li et al. (2018) found that covering 20% of Sahara by solar panels with a 15% conversion efficiency might increase the precipitation rate by 0.53 mm day$^{-1}$ due to intensification of West African monsoon. Thus, Li et al. (2018) showed that the large-scale land surface modifications could affect the continental-scale processes.

Land–sea breeze circulation (LSBC) is a local-scale phenomenon that links to the mesoscale weather processes (Haurwitz 1947; Zolina et al. 2017; Davis et al. 2019; Parajuli et al. 2020). In the coastal regions, the precipitation cycle tends to be affected by the land–sea breeze as well as by the local coastal terrain (Zhu et al. 2017; Mapes et al. 2003; Qian 2008). For example, Qian et al. (2012) found that sea breeze intensity is sensitive to the height of the nearby plateau. Hill et al. (2010) and Davis et al. (2019) analyzed in situ meteorological measurements to characterize the LSBC and its impact on regional climate in the vicinity of the Gulf of Mexico and the Red Sea, respectively. Davis et al. (2019) reported that the Red Sea LSBC is one of the strongest in the world, and influences precipitation and surface temperature regimes in all four seasons of the year, with maximum influence occurring in summer and early autumn (Fig. 1a). Khan et al. (2018) use buoys and meteorological station observations to estimate the RS breeze inland extent length.

The Red Sea is losing approximately 0.9 Tt of water annually to evaporation. This is equivalent to 7.6% of the mass of total atmospheric water vapor (Morcos 1970; Nassir 2012; Trenberth and Smith 2005). In the Red Sea coastal plains, sea breezes transport this water to land areas but little of this
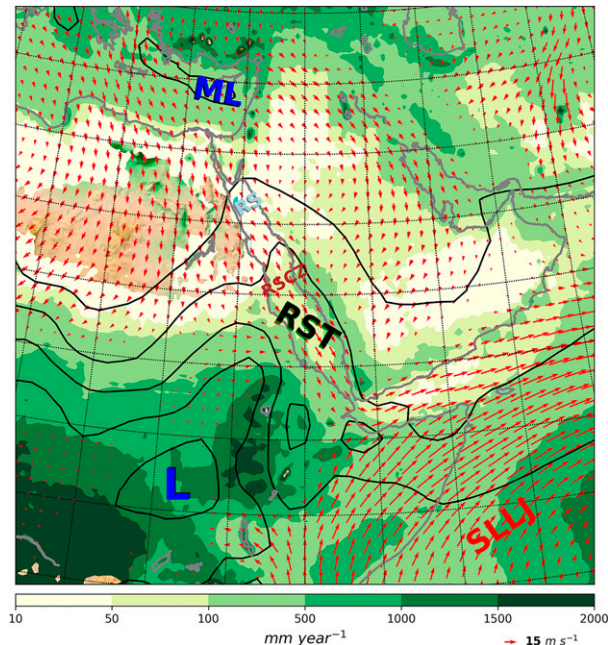
FIG. 1. Regional climatology map. Contours show the mean winter (DJF) sea level pressure (hPa) calculated using ERA20C reanalysis data for 2000–10. The Red Sea trough (RST) stretches out along the Red Sea. Red arrows show the 850-hPa wind (m s$^{-1}$) in summer (JJA) calculated using ERA20C reanalysis data for 2000–10. The Somali low-level jet (SLLJ) blows along the southern coast of the Arabian Peninsula. RSCZ and ML show the locations of the Red Sea convergence zone in winter and Mediterranean low pressure system, respectively. Shading shows the TRMM annual mean precipitation (mm yr$^{-1}$) averaged over 2000–10.

water forms precipitation (Khan et al. 2018; Davis et al. 2019). Instead, most of it returns through the reverse upper branch of breeze circulation and is transported south to the ITCZ.

Given the vast amount of moisture circulating between the Red Sea and the coastal plains, it is practical to explore the feasibility of using this natural process to increase the freshwater supply in the region. This idea was never explored in the past. Therefore, in this study, we aim at evaluating how deliberate changes in land use along the Red Sea coastal line affect the intensity of breeze circulation and the amount of coastal precipitation on regional and local scales over the Arabian Red Sea coastal plain. The science questions we address in this study are as follows:

- How do changes of surface albedo, soil moisture, and afforestation in the Arabian Red Sea coastal plains affect precipitation and surface air temperature?
- How sensitive are the impacts of regional land surface geo-engineering to the size and geographic positioning of a geoengineered region?

To answer these questions, we conduct a series of numerical experiments using the mesoscale WRF regional model with varying land-use types and surface albedo within a limited coastal area. The implication of our study is not restricted

to increasing the freshwater resource. It also develops a scientific and technological basis for evaluating the consequences of large-scale land surface modification in the Middle East. The surface modifications may be associated with building solar and/or wind farms, or tree planting to improve environmental conditions, or large-scale agriculture projects. For example, the Saudi and Middle East Green initiatives launched in March 2021 (https://www.arabnews.com/node/1832861/saudi-arabia) suggest planting 50 billion trees in the Middle East. It is a vast project, the environmental consequences of which should be thorough tested.

## 2. Physics background

### a. Coastal terrain and climatology

The western coast of the AP (and thus the eastern coast of the RS) is located in dry subtropics. It has a semiarid climate with little rainfall, particularly in its northern part (Rasul and Stewart 2015, 595–610; Khan et al. 2018). The Asir Mountains, which run along the coastline, direct the wind along the RS coast. For the entire summer (May–September) the prevailing winds are northwesterly over the whole RS region (Pedgley 1974; Sofianos and Johns 2002; Ralston et al. 2013). However, in the winter (November–April) the so-called Red Sea trough (RST; shown by sea level–pressure contours in Fig. 1), a low (L) pressure system centered in Sudan, combined with a seasonal collapse of the Somali jet, create southeasterly winds in the southern part of the RS. The area where warm southern wind meets a relatively cold northern wind is called the Red Sea convergence zone (RSCZ). Heavy rainfalls and dust storms tend to occur more frequently in this area (Tsvieli and Zangvil 2005; El Kenawy et al. 2014; Awad and Almazroui 2016). North of the RSCZ, the Mediterranean low (ML) pressure system and atmospheric cold front remain the main atmospheric controls. The annual mean precipitation over the RS coastal area is about 90 mm yr$^{-1}$ with the maximum 170 mm yr$^{-1}$ in the south and the minimum 10 mm yr$^{-1}$ in the north (Davis et al. 2019). The RS is one of the warmest and most highly saline aquatic basins on Earth. According to recent observations, the annual average sea surface temperature (SST) of the RS is about 30°C (Chaidez et al. 2017).

Breeze circulation is driven by the high horizontal thermal contrast between land and sea, which creates a pressure gradient force directed from sea to land, and pushes the moist sea air into a shallow layer over the land. Sea breeze circulation occurs when thermal forcing exceeds opposing synoptic-scale forcing (Steyn and Faulkner 1986; Khan et al. 2018). Local topography may block or channel this flow (Miller et al. 2003; Papanastasiou and Melas 2009). When a warm, moist sea air mass meets opposing winds or coastal mountain ranges, it is forced to ascend (Fig. 1a). If there is enough moisture in the air, clouds and precipitation form (Evans and Westra 2012). The inland extent of the breeze scales proportionally to the thermal contrast between sea and land. Khan et al. (2018) analyzed data from five weather stations on the RS eastern coast and found that the maximum inland sea breeze extent is in July (about 200 km) and the minimum is in January (about
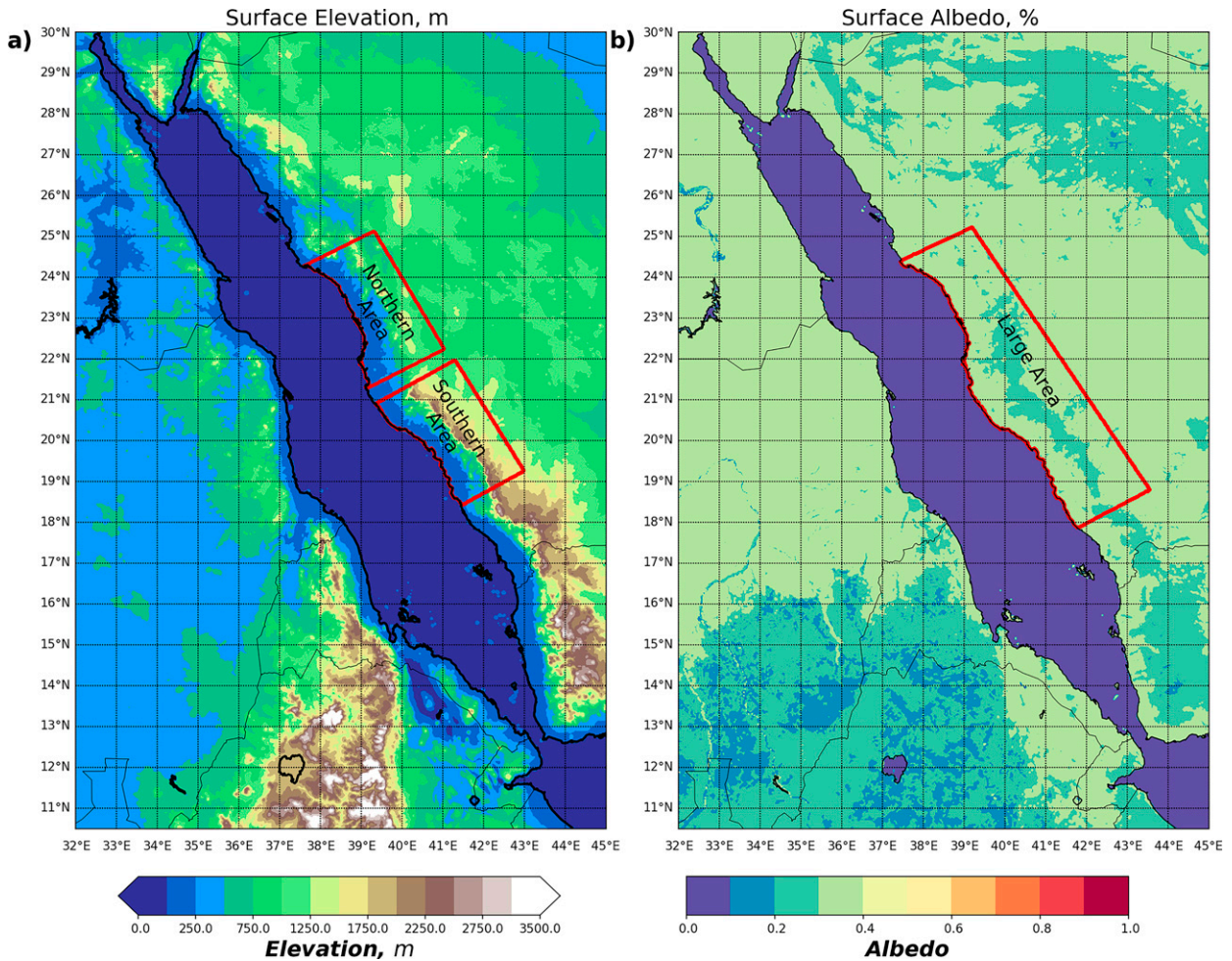
Fig. 2. Simulation domain, geoengineered areas, and distributions of land surface characteristics. (a) Land elevation (m). The red contour lines depict selected northern and southern geoengineered areas used in EXP4, EXP5N and EXP4, EXP5S, respectively. (b) WRF default SW surface albedo. The red contour lines indicate the large geoengineered area used in EXP2, EXP3, EXP4, and EXP5.

150 km). If the temperature and wind speed at the coastline are known, the breeze circulation length BL (inland extent) can be calculated using Eq. (1) (from Pokhrel and Lee 2011):

$$\mathrm{BL} = \frac{0.3429 \times 10^5 h}{T_m \overline{V}} (T_{\mathrm{land}} - T_{\mathrm{sea}}) \qquad (1)$$

where $T_m$ is the mean surface air temperature (K) over the coastline at 2 m above the ground; $\overline{V}$ is mean wind speed

(m s$^{-1}$) at the height of $h = 10$ m; $T_{\mathrm{land}}$ and $T_{\mathrm{sea}}$ are surface air temperatures (K) over land and sea, respectively; and BL is the breeze inland extent (km). From now on, we will use only the terminology "surface temperature" and "surface wind" mean 2-m temperature and 10-m wind, respectively.

### b. Land surface modifications

The vegetation, type of soil, and other components of the terrestrial biosphere influence the climate by controlling

TABLE 1. Model configuration and main physical parameterizations used in the experiments.

| Atmospheric process | WRF options |
| --- | --- |
| Longwave radiation | RRTMG (option 4) scheme (Iacono et al. 2008) |
| Shortwave radiation | RRTMG (option 4) scheme (Iacono et al. 2008) |
| Microphysics scheme | Thompson scheme (option 8) (Thompson et al. 2008) |
| Boundary layer | Mellor–Yamada–Janjić turbulent kinetic energy (TKE) scheme (option 2) (Janjić 1994) |
| Cumulus cloud | Turned off |
| Surface layer | Monin–Obukhov (Janjić) scheme (option 2) (Janjić 1994) |
| Land surface model | Unified Noah land surface model (option 2) (Tewari et al. 2004) |

TABLE 2. Numerical experiments (the default fields can be found in https://www2.mmm.ucar.edu/wrf/users/download/get_sources_wps_geog.html).

| Experiment name | Geoengineered area ($10^3$ km$^2$) | Surface shortwave albedo (%) | Roughness length (cm) | Land cover characteristics | Leaf area index (m$^2$ m$^{-2}$) | Green fraction (%) | Soil moisture (m$^3$ m$^{-3}$) | Notes |
|---|---|---|---|---|---|---|---|---|
| EXP1 | 0 | Default | Default | Default | Default | Default | Default | Reference experiment, done for 2013, 2015, and 2016 |
| EXP2 | 150 | 12 | Default | Wide-leaf forest | 4 | 50 | 0.25 | Afforestation |
| EXP2W | 150 | Default | Default | Default | Default | Default | 0.25 | Soil moisture |
| EXP3 | 150 | 85 | Default | Default | Default | Default | Default | High albedo |
| EXP4 | 150 | 8 | Default | Default | Default | Default | Default | Low albedo, done for 2013, 2015, and 2016 |
| EXP5 | 150 | 20 | Default | Default | Default | Default | Default | Solar panel albedo, done for 2013, 2015 and 2016 |
| EXP4N | 67.5 | 8 | Default | Default | Default | Default | Default | EXP4 northern region |
| EXP4S | 69.0 | 8 | Default | Default | Default | Default | Default | EXP4 southern region |
| EXP5N | 67.5 | 20 | Default | Default | Default | Default | Default | EXP5 northern region |
| EXP5S | 69.0 | 20 | Default | Default | Default | Default | Default | EXP5 southern region |
| EXP5Z | 150 | 20 | 6 | Default | Default | Default | Default | Roughness |

land–atmosphere interaction, namely, the fluxes of latent and sensible heat, momentum, and chemical species between the atmosphere and underlying surface (Bright et al. 2015). Equilibrium surface energy budget can be generalized as

$$R_{SW\downarrow}(1 - \alpha_{SW}) + R_{LW\downarrow}(1 - \alpha_{LW}) - R_{LW\uparrow} = R_G + H + LE, \quad (2)$$

where $\alpha_{SW}$ and $\alpha_{LW}$ are surface shortwave (SW) and longwave (LW) albedos, respectively; $R_{SW\downarrow}$ is downward (to surface) shortwave radiation; $R_{LW\downarrow}$ is downward longwave radiation; $R_{LW\uparrow}$ is upward (to atmosphere) longwave radiation; $R_G$ is in-ground heat flux; $H$ is sensible heat fluxes into the atmosphere; $L$ is specific latent heat of evaporation; $E$ is evaporation; and $LE$ is the latent heat flux from the surface to the atmosphere that comes with water vapor. Strictly speaking, the total evaporated water results from evaporation from bare land and vegetation by evapotranspiration, but here we do not separate these two processes, and refer to them jointly as evaporation $E$. The upward LW radiation flux $R_{LW\uparrow}$ includes both small reflected and emitted LW radiation.

Precipitation driven by mesoscale processes requires multiple complex meteorological, thermodynamic, and circulation mechanisms to work in concert (De Vries et al. 2018, 2013; Tanarhte et al. 2012). It is therefore difficult to predict and control. Instead, we design and conduct numerical experiments, deliberately changing the land surface characteristics on a regional scale to alter the surface energy balance (2) and trigger local precipitation driven by vast moisture flux circulating by sea breezes. The major controls in (2) are latent and sensible heat fluxes, and the surface SW albedo $\alpha_{SW}$. If surface characteristics are altered in a limited area, these changes have potentially little effect on the large-scale environment. The surface LW albedo $\alpha_{LW}$ is small for all types of land cover and therefore it cannot produce a strong effect on precipitation. We do not vary $\alpha_{LW}$ in our simulations.

## 3. Methodology

### a. Model and experimental setup

The Weather Research and Forecasting (WRF) Model is a mesoscale numerical weather prediction system, fully compressible and nonhydrostatic. It is a popular open-source modeling tool that has been used in numerous meteorology

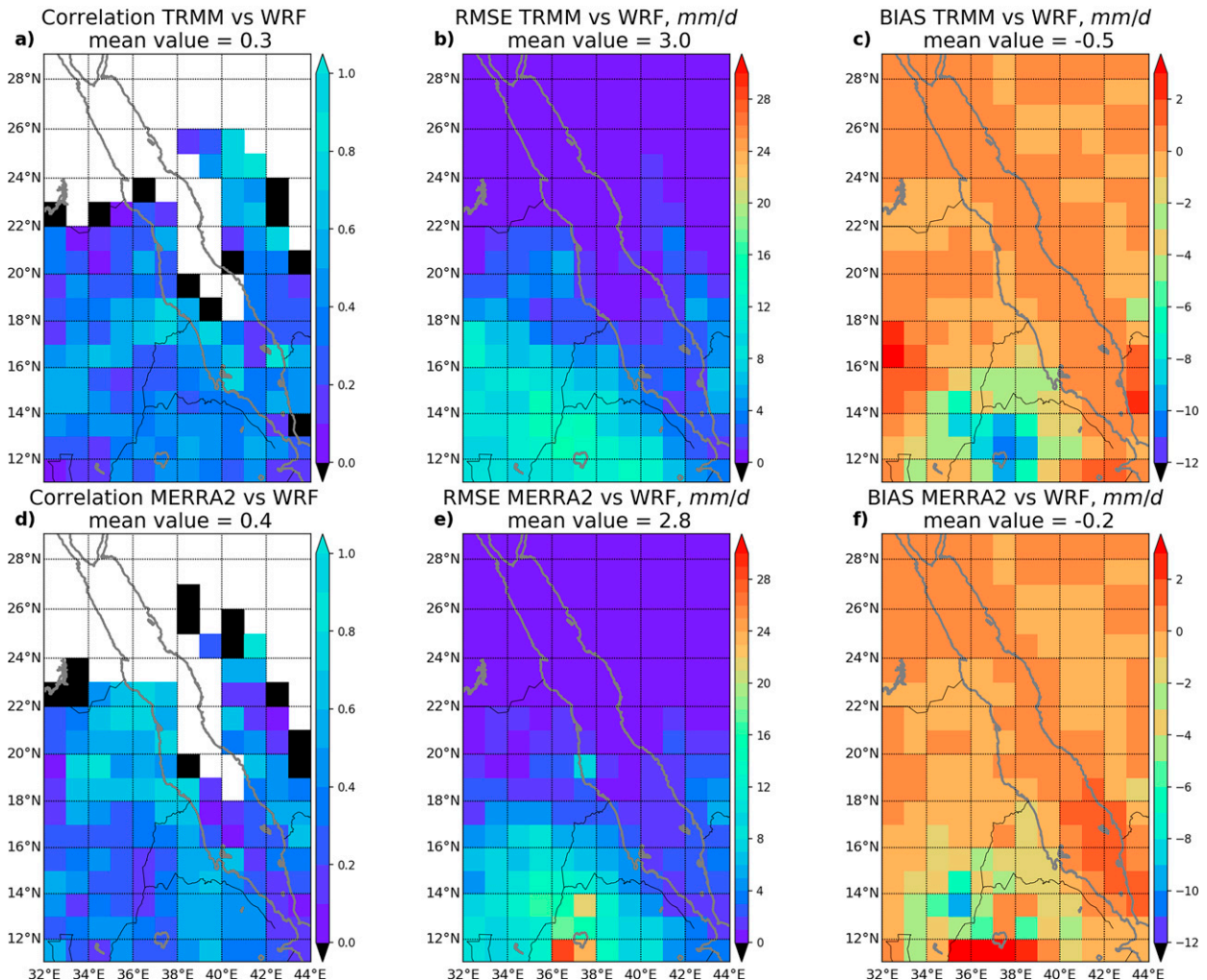## Statistical evaluation of accumulated precipitation



FIG. 3. Comparison of EXP1 daily precipitation rates (mm day$^{-1}$) with TRMM observations and MERRA-2 reanalysis data: (a) the WRF vs TRMM correlation coefficient, (b) WRF vs TRMM root-mean-square error, (c) WRF vs TRMM mean (July–September 2013) bias, (d) WRF vs MERRA-2 correlation coefficient, (e) WRF vs MERRA-2 root-mean-square error, (f) WRF vs MERRA-2 mean (July–September 2013) bias.

and regional climate studies. We use the Advanced Research version of WRF (ARW) dynamics solver (Skamarock et al. 2005) version 3.9.1 that we configured within one domain (Fig. 2), and which covers the RS and its coastal regions. We use Arakawa staggered C-grid (Mesinger and Arakawa 1976) with a horizontal resolution of $3 \times 3$ km$^2$ in the WRF Model domain with an area of $39 \times 10^5$ km$^2$ to approximate meteorological processes, with 575 grid points along the latitude and 750 grid points along the longitude. The vertical structure of meteorological flows is approximated on 50 model levels, 25 of which are located in the planetary boundary layer (PBL), which in the desert reaches 5–6-km height (Parajuli et al. 2020). We use the Lambert conformal conic (LCC) geographic projection (Brown 1935; Snyder 1978).

To ensure that large-scale meteorological processes are correctly captured in our simulations, we use spectral nudging of zonal and meridional wind components above the desert PBL ($z > 5$ km) with a characteristic time of 10 000 s (Miguez-Macho et al. 2004). We nudge only the 10 largest modes in the free troposphere, which preserves large-scale meteorological forcing and allows the model to develop its own small-scale processes in the boundary layer.

To simulate local meteorology accurately, land use and other static fields should be of a high spatial resolution (Sertel et al. 2010; De Meij and Vinuesa 2014; Baklanov et al. 2008). Therefore, we assembled the fields of land-use static parameters such as albedo, surface roughness, and vegetation cover using U.S. Geological Survey (USGS) land cover data
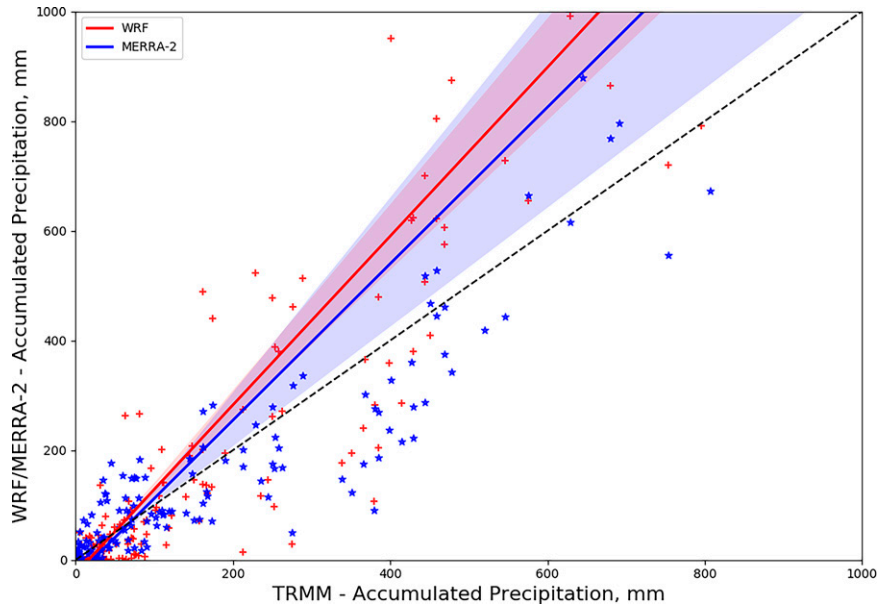
FIG. 4. Scatter diagram of EXP1 (red) and MERRA-2 (blue) showing accumulated (July–September 2013 in model grid boxes) precipitation (mm) vs TRMM gridded observations. Solid lines are regression curves with shaded 95% confidence intervals.

(Davidson and McKerrow 2016) with an effective spatial resolution of 1 km.

To describe land surface processes and calculate energy exchange between the land and the atmosphere, we employ the Noah land surface model (Tewari et al. 2004). For radiation transfer calculations, we use the Rapid Radiative Transfer Model (RRTM) for both the SW and LW spectral bands. A list of the main physical parameterizations used in our experiments is presented in Table 1.

To calculate meteorological initial and boundary conditions, we use the ECMWF operational analysis (F1280) fields with a spatial resolution of 9 km $\times$ 9 km and a temporal resolution of 6 h.

We designed 10 numerical experiments (Table 2) to explore the effect of land-use changes on precipitation over the Arabian coastal Red Sea plain. For this we chose three geoengineered areas [large, northern, and southern (Fig. 2a)] that cover the parts of the coastal plain with low summer precipitation (less than 0.3 mm day$^{-1}$ on average) in the north, and areas with relatively high summer precipitation in the south. The width of the geoengineered area was chosen on the assumption that the breeze inland extent length is of the order of 200 km (Khan et al. 2018).

The control or reference experiment (EXP1) was calculated using the model default settings from Table 1. In EXP2 we converted $150 \times 10^3$ km$^2$ of bare land in the large selected area (Fig. 2a) to wide-leaf forest with 50% tree density, meaning 50% of each grid cell in the selected area was covered with wide-leaf trees. It would require about 1 billion trees to cover this area, 10% of what is suggested to plant in the course of the Saudi Green Initiative (https://www.arabnews.com/node/1832861/saudi-arabia). The surface albedo, soil moisture, and leaf area index (LAI) were changed accordingly

(Table 2). In EXP2W we changed only soil moisture, just as in the wide-leaf forest EXP2, keeping all other surface parameters identical to the control run. To assess the effect of surface albedo, three simulations EXP3, EXP4, and EXP5 were performed by modifying the albedo over the selected large area. We imposed a high land surface albedo of 0.85 in EXP3, which mimics the albedo of white sand; a low surface albedo of 0.08, which mimics the ocean albedo in EXP4; and an intermediate albedo of 0.2 in EXP5, which mimics the effect of solar panels on surface energy balance (2). To study the effects of topography, size, and geographic position of the geoengineered region on precipitation, we applied the same surface modifications as in EXP4 and EXP5 to the smaller northern and southern areas (Fig. 2b). The northern area, where the mountain range lies far from the coastline, has a terrain height of about 1 km. In the southern area, where the mountain range is closer to the coastline, the terrain height exceeds 2 km. We refer to these experiments as EXP4N, EXP5N, EXP4S, and EXP5S (Table 2). We designed additional experiment EXP5Z to study sensitivity to surface roughness length.

We chose the summer (July–September) season of 2013 for our simulations. Summer in the AP is the driest season (Climatestotravel.com 2021). There is almost no precipitation in the northwestern coastal area of the AP. The inland extent of the sea breeze circulation and the frequency of its occurrence are at their maximum during the summer (Khan et al. 2018; Davis et al. 2019). To test how interannual variability affects the results, we repeated EXP1, EXP4, and EXP5 for the summers of 2015 and 2016.

We run simulations for three months with a 1-week spinup on the KAUST supercomputer (CRAY-XC40) using 128

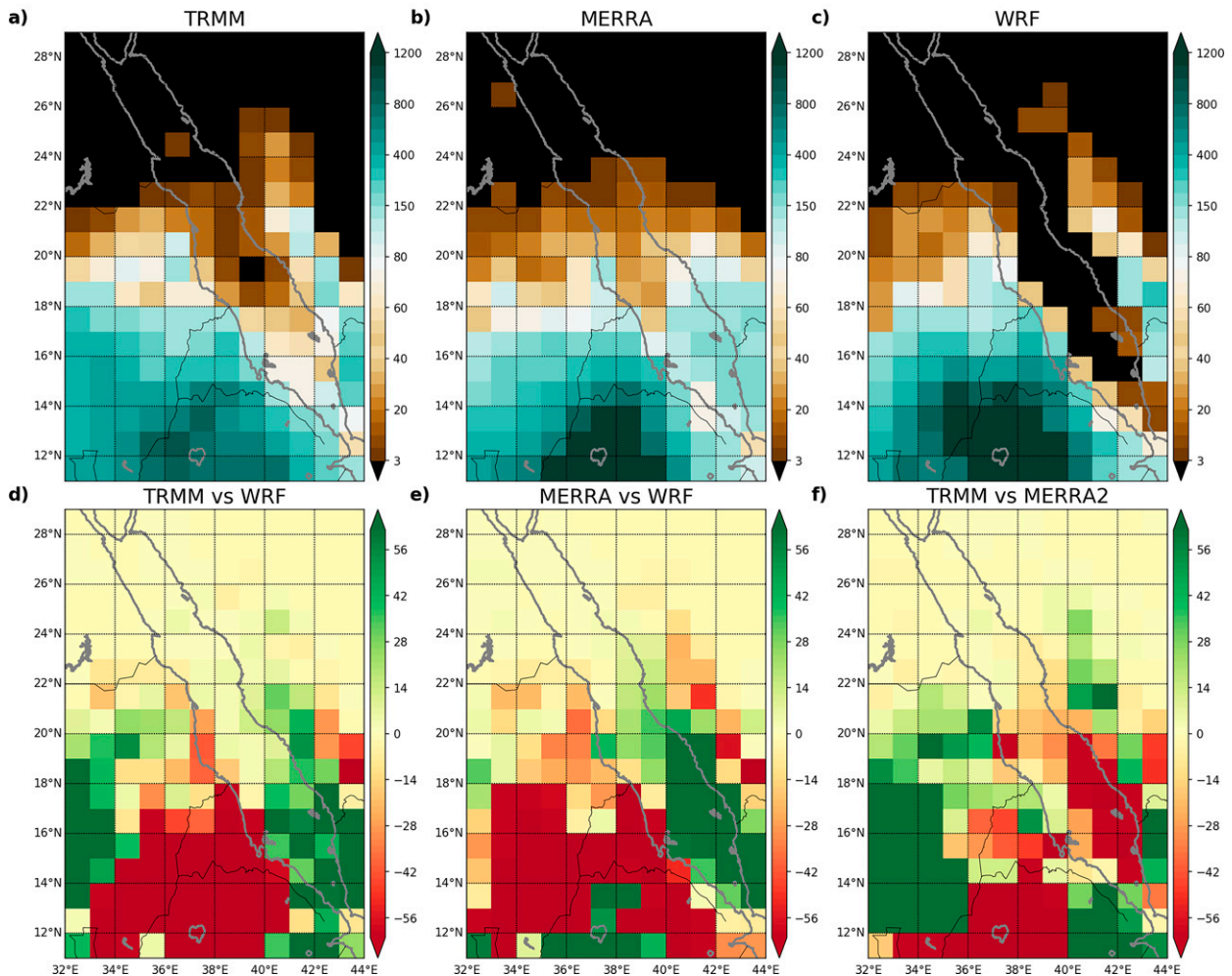## Accumulated Precipitation, mm (July - September 2013)



FIG. 5. Spatial distribution of accumulated precipitation (mm) from EXP1 and MERRA-2 and TRMM gridded observation: (a) TRMM, (b) MERRA-2, (c) WRF, (d) difference of TRMM − WRF, (e) difference of MERRA-2 − WRF, (f) difference of TRMM − MERRA-2.

nodes (each node has 32 cores). It takes 8–10 CPU hours for each simulation. We report the results from this entire period of simulations, excluding the 1-week spinup time at the simulations' beginning.

TABLE 3. Pearson correlation coefficient ($r$), root-mean-square error (RMSE), and absolute and relative biases (BIAS) calculated for the 3 months accumulated precipitation fields for the WRF and MERRA-2 fields with respect to TRMM observations, as well as the difference between MERRA-2 and WRF accumulated precipitation. The relative biases are calculated with respect to the observed TRMM accumulated precipitation of 130 mm.

|              | $r$  | RMSE (mm) | BIAS (mm)    |
|--------------|------|-----------|--------------|
| MERRA-2–WRF  | 0.88 | 170       | 16.1 (12%)   |
| WRF–TRMM     | 0.89 | 157       | 8.7 (6%)     |
| MERRA-2–TRMM | 0.83 | 216       | 24.7 (18%)   |

### b. Data

To initiate simulations and evaluate model results, we use data from the Modern-Era Retrospective Analysis for Research and Applications version 2 (MERRA-2) reanalysis (Randles et al. 2017), observations from the Tropical Rainfall Measuring Mission (TRMM) (Liu et al. 2012), and high-resolution meteorological fields from the European Centre for Medium-Range Weather Forecasts (ECMWF) operational analysis.

The MERRA-2 dataset provides 3D gridded meteorological (reanalysis) data on a latitude–longitude grid with a horizontal resolution of 0.625° × 0.50° and 72 sigma hybrid levels (Randles et al. 2017; Buchard et al. 2017). MERRA-2 interactively calculates dust generation, transport, and its radiative forcing, which improves rainfall simulations in the Middle East where the dust effect is of primary importance. In this study, we use MERRA-2 three-hour total precipitation fields to evaluate model output. MERRA-2 data were obtained from https://gmao.gsfc.nasa.gov/reanalysis/MERRA2/.
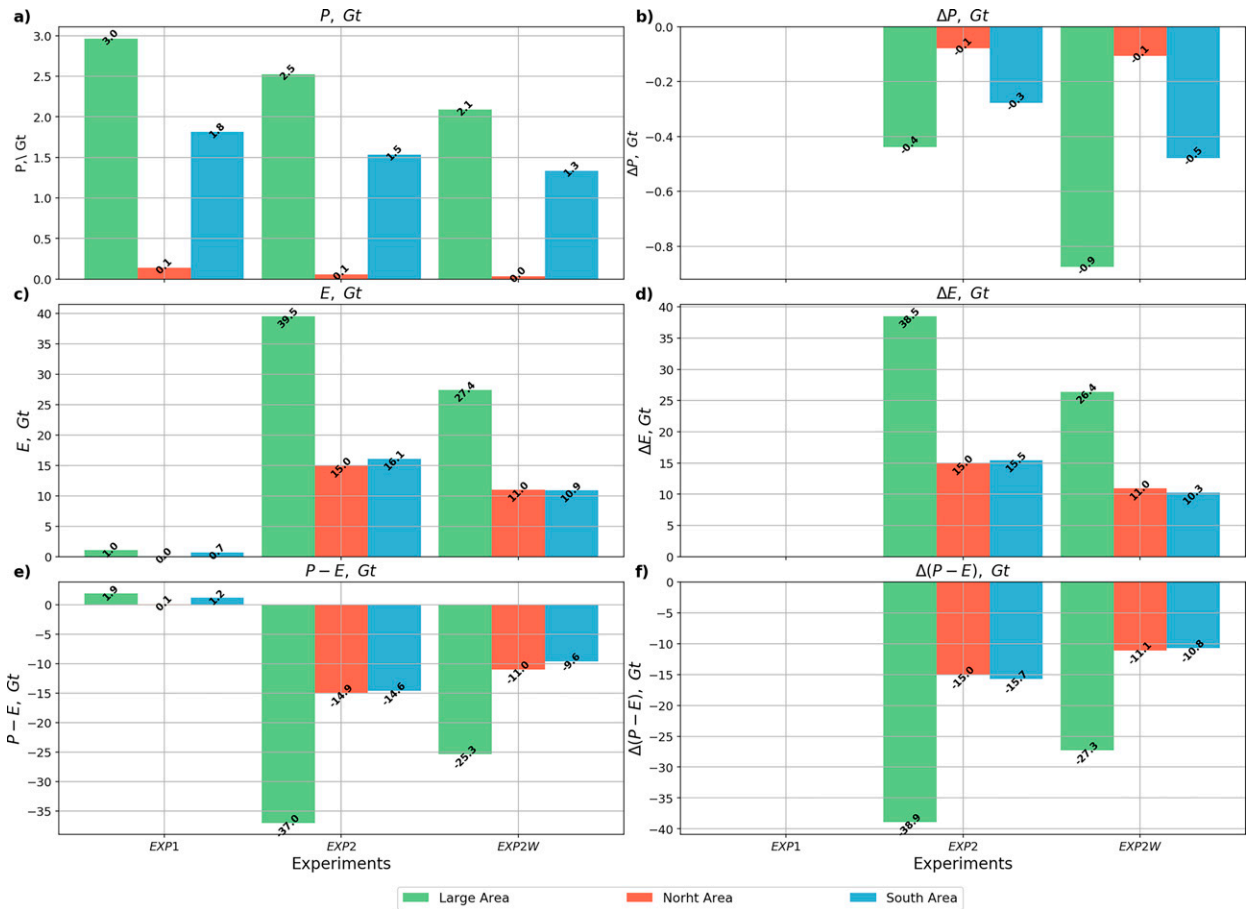
FIG. 6. Accumulated (for summer 2013) precipitation $P$, evaporation $E$, and $P - E$ integrated over the large (green), northern (red), and southern (blue) geoengineered areas (Gt) in EXP1, EXP2, and EXP2W: (a) $P$, (c) $E$, (e) $P - E$. Change of accumulated precipitation $\Delta P$, evaporation $\Delta E$, and $\Delta(P - E)$ integrated over large (green), northern (red), and southern (blue) geoengineering areas (Gt) in EXP2 and EXP2W with respect to EXP1: (b) $\Delta P$, (d) $\Delta E$, (f) $\Delta(P - E)$.

The TRMM was a joint space mission between the National Aeronautics and Space Administration (NASA) and the Japan Aerospace Agency (JAXA) designed to monitor and study tropical rainfall. Operating until 2015, TRMM collected 17 years of data. The TRMM was conducted through the operation of five instruments: a three-sensor rainfall suite [Precipitation Radar (PR), TRMM Microwave Imager (TMI), Visible and Infrared Scanner (VIRS)], and two related instruments [Lightning Imaging Sensor (LIS) and Clouds and the Earth's Radiant Energy Sensor (CERES)]. The gridded (25 km × 25 km) TRMM data with 3-h temporal resolution can be downloaded from http://disc.sci.gsfc.nasa.gov/precipitation/documentation/TRMM_README/TRMM_3B42_readm. In this study we use the CERES (3B42RT) dataset. A detailed description of TRMM data can be found in Huffman et al. (2007).

The Integrated Forecast System (IFS) of the ECMWF uses a semi-Lagrangian model with 137 vertical levels (L137) up to 0.01 hPa. The spectral approximation in the horizontal plane with triangular truncation at wavenumber 1279 (T1279) is employed for upper-air fields and horizontal derivatives. Dynamic tendencies and diabatic physical parameterizations

are calculated on a Gaussian horizontal grid. This setup corresponds to a horizontal grid spacing of ~9 km. IFS provides 10-day forecasts four times a day from an initial state produced via four-dimensional variational data assimilation, dynamically combining a short-range forecast with observational data. It operationally makes analyses for 0000, 0600, 1200, and 1800 UTC (= +3 LST) every day (ECMWF 2016). ECMWF operational analysis can be downloaded from https://apps.ecmwf.int/archive-catalogue/?type=an&class=od&stream=oper&expver=1.

## 4. Results

### a. Model evaluation

We tested the modeled precipitation against reanalysis and available observations. Since ECMWF operational analysis was employed to calculate initial and boundary condition, we did not use this dataset for the verification of precipitation fields, and instead chose the independent TRMM observations and MERRA-2 reanalysis output for this purpose. To
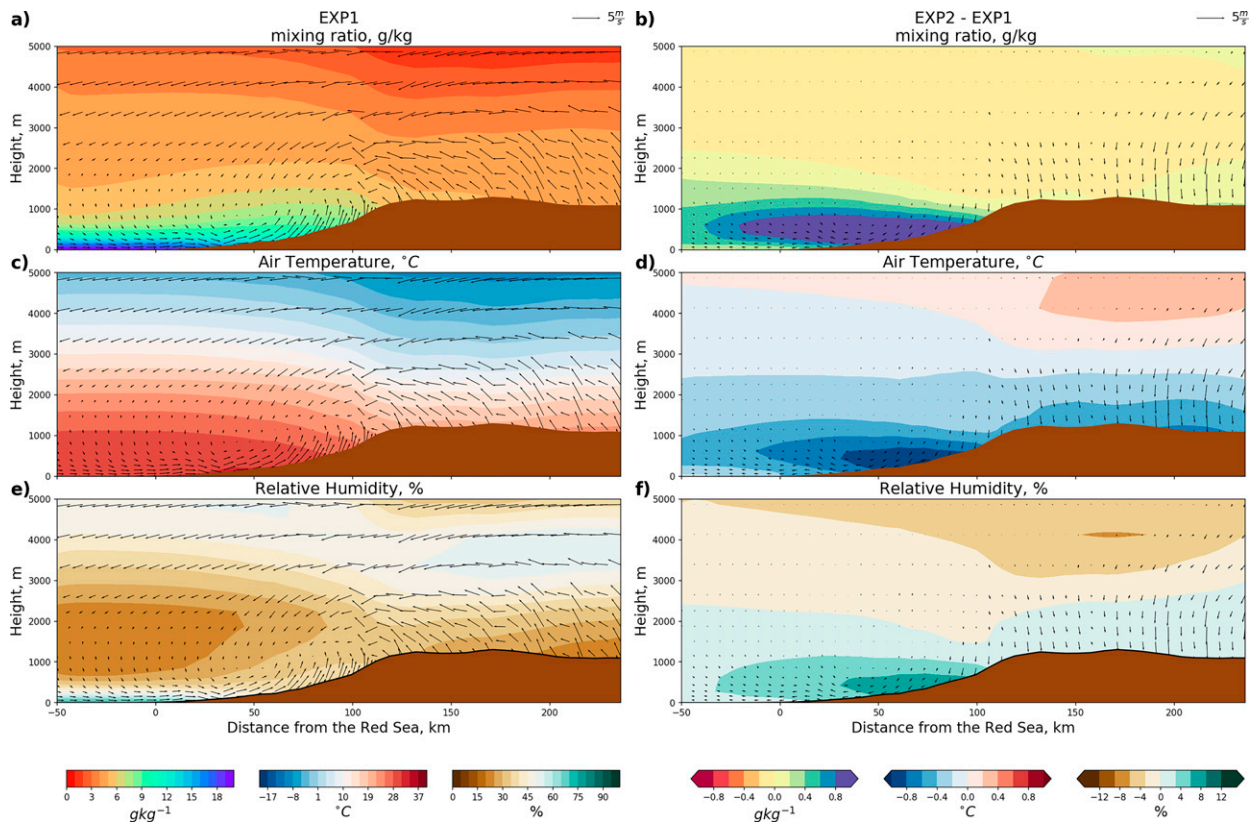
FIG. 7. Vertical cross section of the mean (July–September 2013) meteorological characteristics averaged along the coastal line within the large geoengineered area. (a) Water vapor mixing ratio (g kg$^{-1}$) and wind vectors (m s$^{-1}$) for EXP1. (b) As in (a), but for the difference of EXP2 − EXP1. (c) Air temperature (°C) and wind vectors (m s$^{-1}$) for EXP1. (d) As in (c), but for EXP2 − EXP1. (e) Relative humidity (%) and wind vectors (m s$^{-1}$) for EXP1. (f) As in (e), but for EXP2 − EXP1.

conduct statistical analysis, we interpolated all of the fields onto the same unified grid using a conservative interpolation scheme (Bonelle et al. 2018). Since the subject of our research is precipitation, we have presented here only a temporal and spatial statistical evaluation of the model primarily for precipitation fields. The model's temporal bias, root-mean-square error (RMSE), and Pearson correlation coefficient ($r$) for daily precipitation fields with respect to TRMM observations are shown in Figs. 3a–3c. The differences between the model and observational values are generally small (<0.3 mm day$^{-1}$) with slightly dry biases in the areas with a low precipitation rate, mostly on the eastern coast of the RS. The maximum dry (2–4 mm day$^{-1}$) and wet (8–10 mm day$^{-1}$) biases are seen over Africa, in the region with heavy precipitation related to the ITCZ, with an average precipitation rate of 12–15 mm day$^{-1}$. In the southern part of the RS coastal plain, where orographic precipitation over the local topography reaches 3 mm day$^{-1}$ (Abdullah and Al-Mazroui 1998), the model results exhibit a dry bias of 1 mm day$^{-1}$. Figures 3d–3f show a temporal correlation coefficient, RMSE, and the bias of daily precipitation from WRF with respect to MERRA-2. The results are very similar to those of the WRF versus TRMM comparison.

We also evaluated the temporal and spatial patterns of the 3-month accumulated precipitation in WRF by comparing the simulated fields with the TRMM observations and the MERRA-2 reanalysis. Figure 4 compares accumulated precipitation in different grid cells, both as simulated by the model and as observed by TRMM. It demonstrates a generally good agreement between simulated precipitation and that observed by TRMM. Light 3-month cumulative precipitations (<200 mm) in WRF and MERRA-2 are well correlated with TRMM. However, WRF overestimates heavy precipitation. Figure 5 confirms that the model captures the spatial distribution of accumulated precipitation over land, but shows disagreement with observations over the RS. The WRF simulated average amount of precipitation over the domain is 138 mm. It is closer to TRMM (130 mm) than MERRA-2 (154 mm). The statistical characteristics of accumulated precipitation fields (Table 3) show that WRF reproduces the precipitation patterns well, and that the model results are in better agreement with TRMM than MERRA-2. The worse statistical scores of the MERRA-2 rainfall when compared with WRF simulations are due to the fact that MERRA-2 is a global reanalysis. It has a much lower spatial resolution than our regional-model simulations and cannot accurately describe the near-coast processes (Zolina et al. 2017).
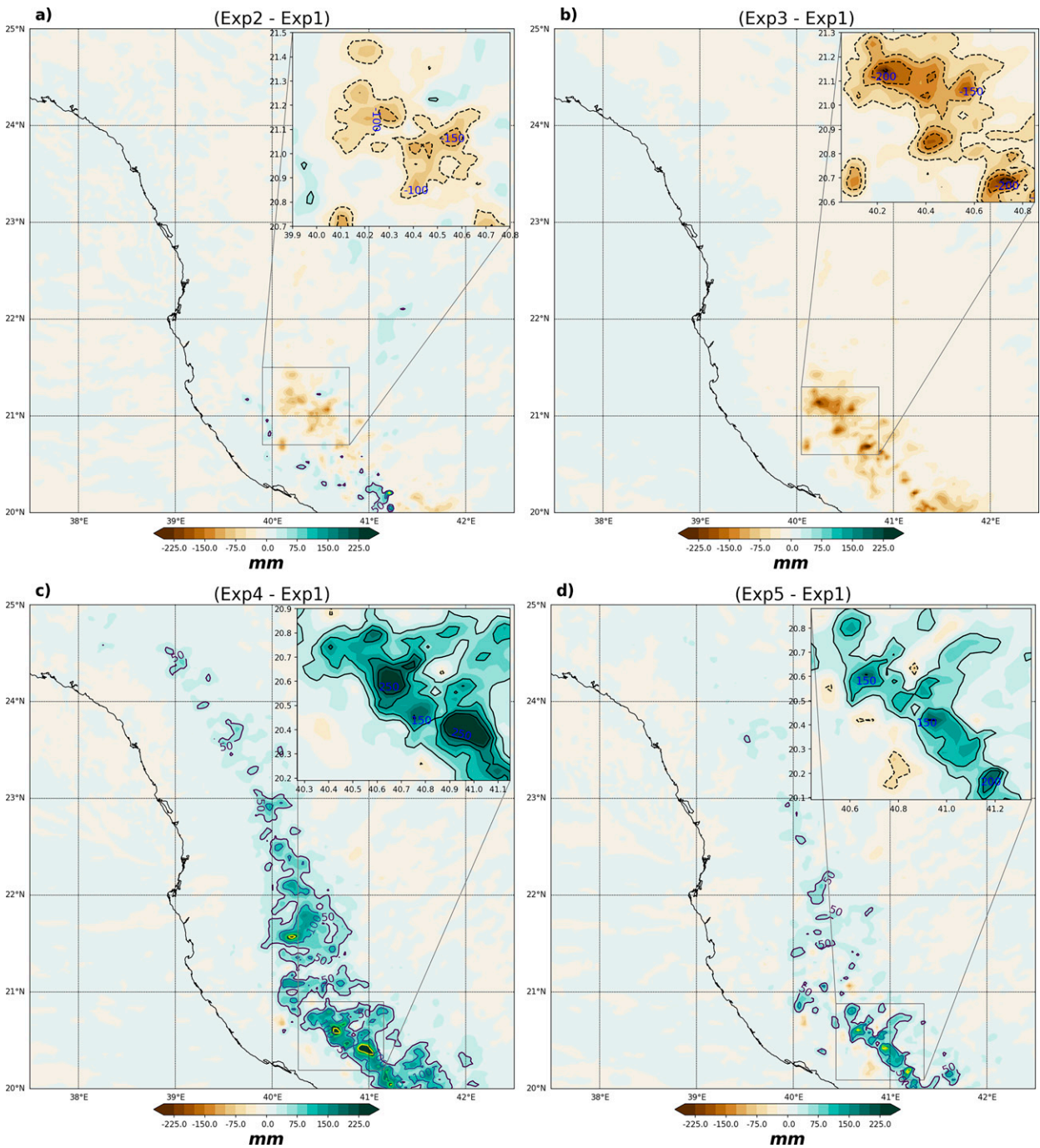
FIG. 8. Change of accumulated (July–September 2013) precipitation (mm) in EXP2, EXP3, EXP4, and EXP5 with respect to EXP1: (a) EXP2 − EXP1, (b) EXP3 − EXP1, (c) EXP4 − EXP1, (d) EXP5 − EXP1.

## b. Geoengineering scenarios

### 1) EVAPORATION CONTROL

In EXP2 we converted $150 \times 10^3$ km$^2$ of bare land in the large geoengineered area (Fig. 2a) into a broadleaf forest (Table 2).

Trees transpire large amounts of water consuming only a small portion of it (about 5%) for their metabolism (Sinha 2004). We assume the soil moisture of the upper soil layer is maintained at least at 25% by irrigation. This is a minimum value necessary to sustain broadleaf trees, as they cannot be sustained if soil
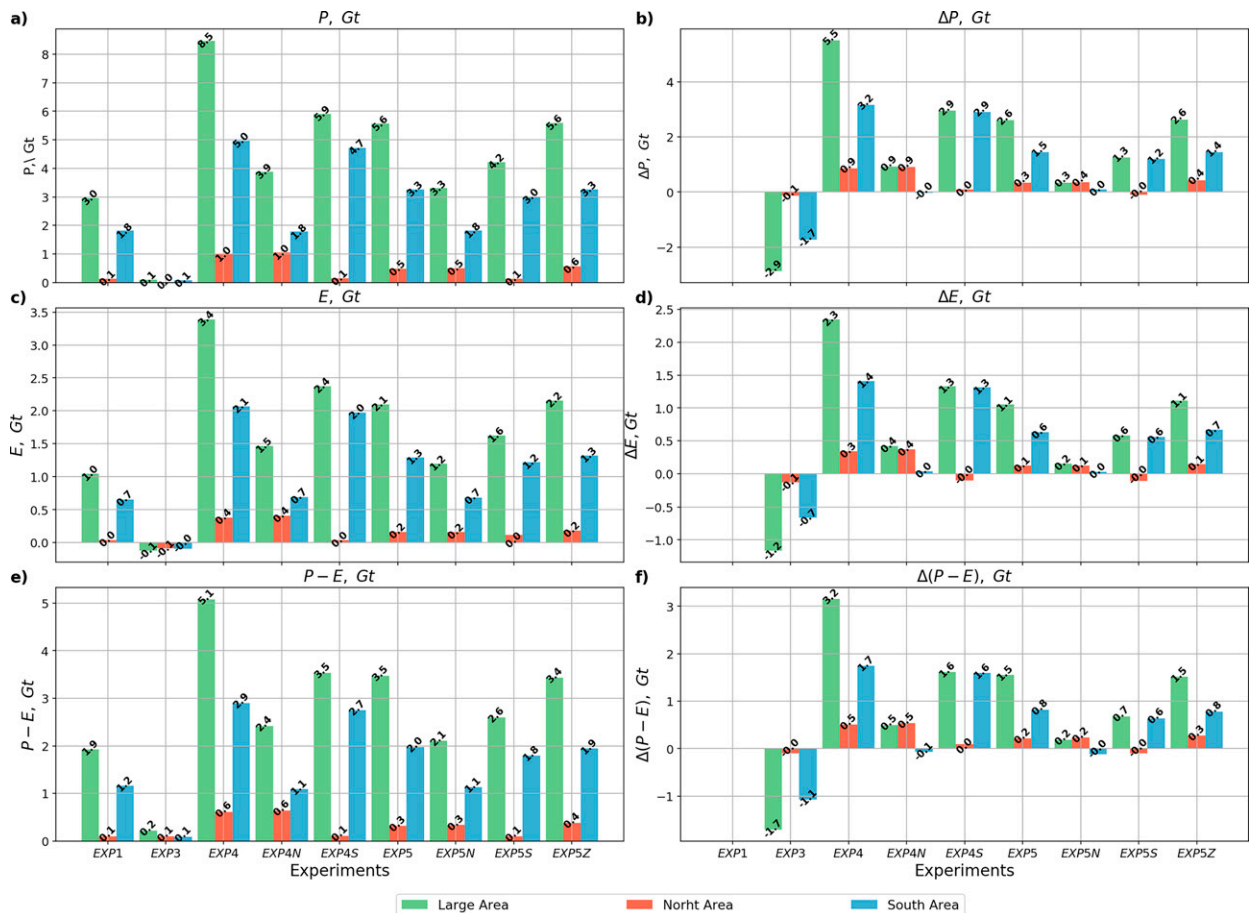
FIG. 9. Accumulated (July–September 2013) precipitation $P$, evaporation $E$, and $P - E$ integrated over the large (green), northern (red), and southern (blue) geoengineered areas (Gt) in EXP1, EXP3, EXP4, EXP5, EXP4N, EXP4S, EXP5N, and EXP5S: (a) $P$, (c) $E$, (e) $P - E$. Change of accumulated precipitation $\Delta P$, evaporation $\Delta E$, and $\Delta(P - E)$ integrated over large (green), northern (red), and southern (blue) geoengineering areas (Gt) in EXP3, EXP4, EXP5, EXP4N, EXP4S, EXP5N, and EXP5S with respect to EXP1: (b) $\Delta P$, (d) $\Delta E$, (f) $\Delta(P - E)$.

moisture decreases significantly below this level. A water balance $(P - E)$ characterizes the net freshwater gain. The left column in Fig. 6 shows the cumulative precipitation, evaporation, and their differences for both the reference and perturbed experiments (Table 2), integrated over the large and small geoengineered regions. The right column shows the changes in these parameters in comparison with EXP1. In EXP2 evaporation significantly increases but precipitation $P$ decreases. As a result, the soil water balance $(P - E)$ is negative. It would require 36.9 Gt of water to maintain the forest for the 85-day period of the simulations (Fig. 6f), which is almost 4 times the annual water consumption of Saudi Arabia.

This is counterintuitive, since accumulated evaporation from the large afforested area is 39.5 Gt (Fig. 6c), which provides moisture to the atmosphere that could be recycled for precipitation. The forested area has lower albedo than bare land (Swann et al. 2012) and therefore absorbs more solar radiation. However, the latent heat cooling prevails and surface temperature decreases. This leads to a weakening of breeze circulation and shutting down of the moisture flux from the RS, which appears to be more important for

formation of coastal precipitation than the recycling of added evaporation. Figure 7 shows the wind vectors, water vapor, air temperature, and relative humidity in the control run, EXP1, and their changes in EXP2 with respect to the control run. The fields are averaged along the RS coast in the vertical cross section that is perpendicular to the coastline. The time averaging was performed during the daytime from 0600 to 1800 UTC when sea breeze is active (Khan et al. 2018).

In EXP1 sea breeze in-land propagation is approximately 150–200 km (Figs. 7a,c,e). This inland propagation is consistent with observations (Khan et al. 2018; Davis et al. 2019). The vertical extent of breeze circulation reaches 3 km, almost 5 times higher than in midlatitude breezes, due to strong surface heating and ascending coastal terrain. Figures 7b, 7d, and 7f show the increasing of the water vapor mixing ratio in EXP2 by up to 1 g kg$^{-1}$, and relative humidity by 5% on the slopes of nearshore mountains. However, temperature over land decreases by 1 K, and breeze circulation significantly weakens. This damping of the breeze leads to a decrease in precipitation in the coastal plain (Fig. 8a).
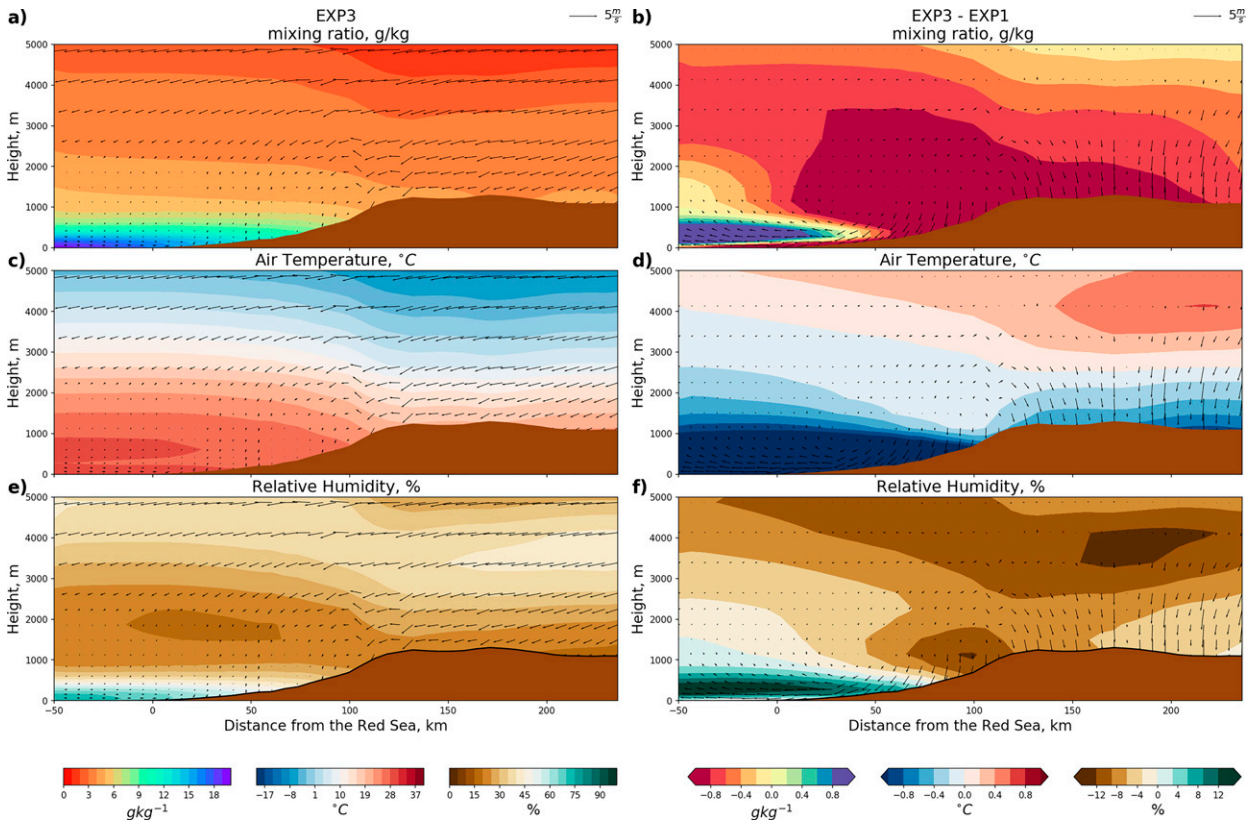
FIG. 10. Vertical cross section of the mean (July–September 2013) meteorological characteristics averaged along the coastal line within the large geoengineered area. (a) Water vapor mixing ratio (g kg$^{-1}$) and wind vectors (m s$^{-1}$) for EXP3. (b) As in (a), but for EXP3 − EXP1. (c) Air temperature (°C) and wind vectors (m s$^{-1}$) for EXP3. (d) As in (c), but for EXP3 − EXP1. (e) Relative humidity (%) and wind vectors (m s$^{-1}$) for EXP3. (f) As in (e), but for EXP3 − EXP1.

The spatial effect of afforestation on the amount of accumulated precipitation is shown in Fig. 8a, which depicts the difference in accumulated precipitation in EXP2 and EXP1. The strongest decrease of accumulated precipitation exceeds 150 mm in the southern part of the selected region (south of 22.2°N, where breezes interact with the steep terrain, triggering precipitation. When breezes weaken, this process ceases. In the northern part of the coastal plain the decrease of cumulative precipitation reaches 40–50 mm. We

observe a slight increase of precipitation in the southwest of the Arabian Peninsula, as well as in southern Yemen (out of domain). In summary, the increase of evaporation is the primary driving mechanism in the afforestation experiment which leads to surface cooling. The net effect is complicated because the afforestation simultaneously changes both surface albedo and evaporation. To better demonstrate the evaporation mechanism, we designed the more straightforward experiment EXP2W, where soil moisture alone is changed to 25% in the geoengineered area, and land use and surface albedo remain the same as in the control run. Watering of bare soil was previously attempted to dampen dust generation (Fitz and Bumiller 2000). The results from EXP2W are very similar to those of EXP2. However, the evaporation over bare land is smaller than over the forested area. It requires only 25.3 Gt of water for soil watering per season (compared to 37 Gt of water required to maintain a broadleaf forest) to maintain soil moisture at 25%, while forested area requires 37 Gt of water (Fig. 6). Intensified latent heat flux cools the surface by about 1 K, damps breeze circulation, and decreases precipitation over the geoengineered area.

TABLE 4. Numerical estimation of land–sea breeze length (BL); $\overline{T_{2m}}$ is the mean surface air temperature (K) at the coastline, $\overline{V_{10m}}$ is mean surface wind speed (m s$^{-1}$), $\overline{T_{land}}$ and $\overline{T_{sea}}$ are surface air temperatures over land and sea, respectively, $\overline{\Delta T}$ is the difference of surface air temperature over land and sea; and $\overline{BL}$ is the breeze inland extent.

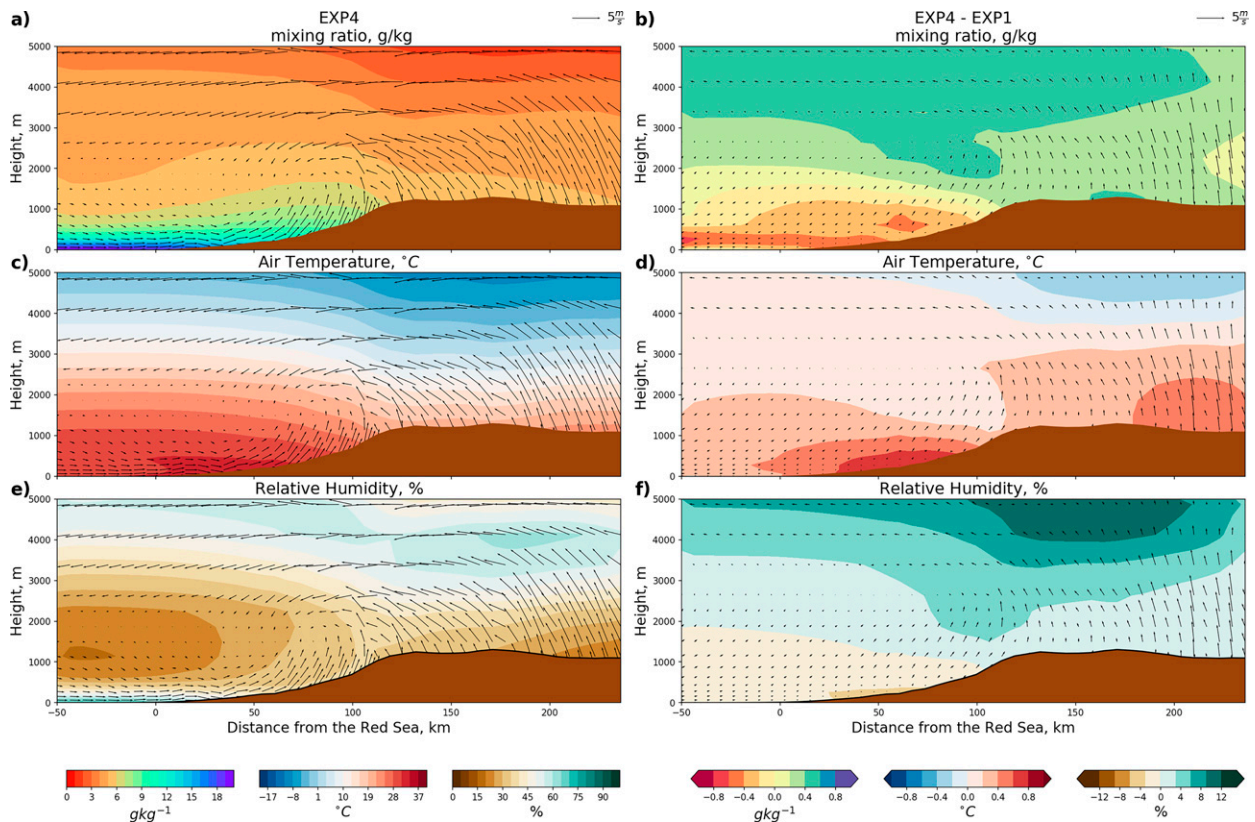| Experiments | $\overline{T_{2m}}$ | $\overline{V_{10m}}$ | $\overline{T_{land}}$ | $\overline{T_{sea}}$ | $\overline{\Delta T}$ | $\overline{BL}$ |
|---|---|---|---|---|---|---|
| EXP1 | 305.2 | 4.6 | 307.1 | 304.1 | 3.0 | 147 |
| EXP2 | 304.1 | 1.5 | 304.5 | 303.9 | 0.6 | 91 |
| EXP3 | 303.9 | 2.1 | 301.6 | 303.4 | −1.9 | None |
| EXP4 | 305.5 | 3.4 | 308.3 | 304.3 | 4.1 | 266 |
| EXP5 | 305.4 | 3.2 | 307.9 | 304.2 | 3.7 | 261 |

FIG. 11. Vertical cross section of the mean (July–September 2013) meteorological characteristics averaged along the coastal line within the large geoengineered area. (a) Water vapor mixing ratio (g kg$^{-1}$) and wind vectors (m s$^{-1}$) for EXP4. (b) As in (a), but for EXP4 − EXP1. (c) Air temperature (°C) and wind vectors (m s$^{-1}$) for EXP4. (d) As in (c), but for EXP4 − EXP1. (e) Relative humidity (%) and wind vectors (m s$^{-1}$) for EXP4. (f) As in (e), but for EXP4 − EXP1.

### 2) Surface albedo control

Surface albedo is another parameter which controls the energy balance of the surface. It is linked to the type of vegetation and land cover properties, but in the model can also be changed independently. Modification of albedo has been proposed as a means to control temperature in different environments. For example, painting the roofs of buildings white has been suggested as a way to decrease solar heating in urban areas (Ismail et al. 2011). Selection of crops with higher albedo has also been proposed to decrease temperature in rural regions (Pongratz et al. 2012). In this context, we changed the albedo of the land surface to explore its effect on surface temperature, breeze circulation, and precipitation in the Arabian coastal plains.

In EXP3 we sat surface albedo to 0.85, aiming to reduce absorption of solar radiation, cool the surface, and increase orographic precipitation. Similarly to EXP2 and EXP2W, the effect on precipitation appears to be negative, as breeze circulation breaks due to land cooling by 5°–7°C (Fig. 8b vs Fig. 9). Figure 10 demonstrates that sea breeze circulation is reversed to a land breeze circulation. The time-averaged maximum 2-m land temperature in EXP3 is decreased to 301 K, giving a negative land–sea temperature contrast of −1.9 K (Table 4). Therefore, the wind flow direction reverses and heads from land to sea. The

vertical extent of high water vapor mixing ratio decreases in comparison with EXP1 (Fig. 10b). Maximum water vapor mixing ratio over land is now located within a shallow layer of 400–500 m. The amount of both precipitation and evaporation in EXP3 decrease to almost zero (Figs. 9a,c). Thus, afforestation, watering of land surface, and increase of surface albedo exhibit similar weakening of the sea breeze circulation, and all these modifications have an adverse effect on precipitation.

In EXP4, we decreased surface albedo of the entire region to 0.08. Contrary to EXP2, EXP2W, and EXP3, this warms the land and intensifies sea breezes due to increased land–sea temperature contrast. Warming over land triggers shallow convection and intensifies vertical mixing, thus altering the land–atmosphere fluxes of momentum, moisture, and heat, which in turn feeds back into breeze circulation and cloud formation and affects the local precipitation (Figs. 8c and 11). The strengthening of near-surface vertical wind due to stronger onshore flow also excites Kelvin–Helmholtz instability and hence turbulence in the boundary layer (Drobinski et al. 2006).

The most notable feature in EXP4 is the more intensive vertical mixing of water vapor in comparison with EXP1 (Fig. 11b). The high water vapor mixing ratio in EXP4 extends up to 5 km, while in the control run it was confined within the lower 3-km layer
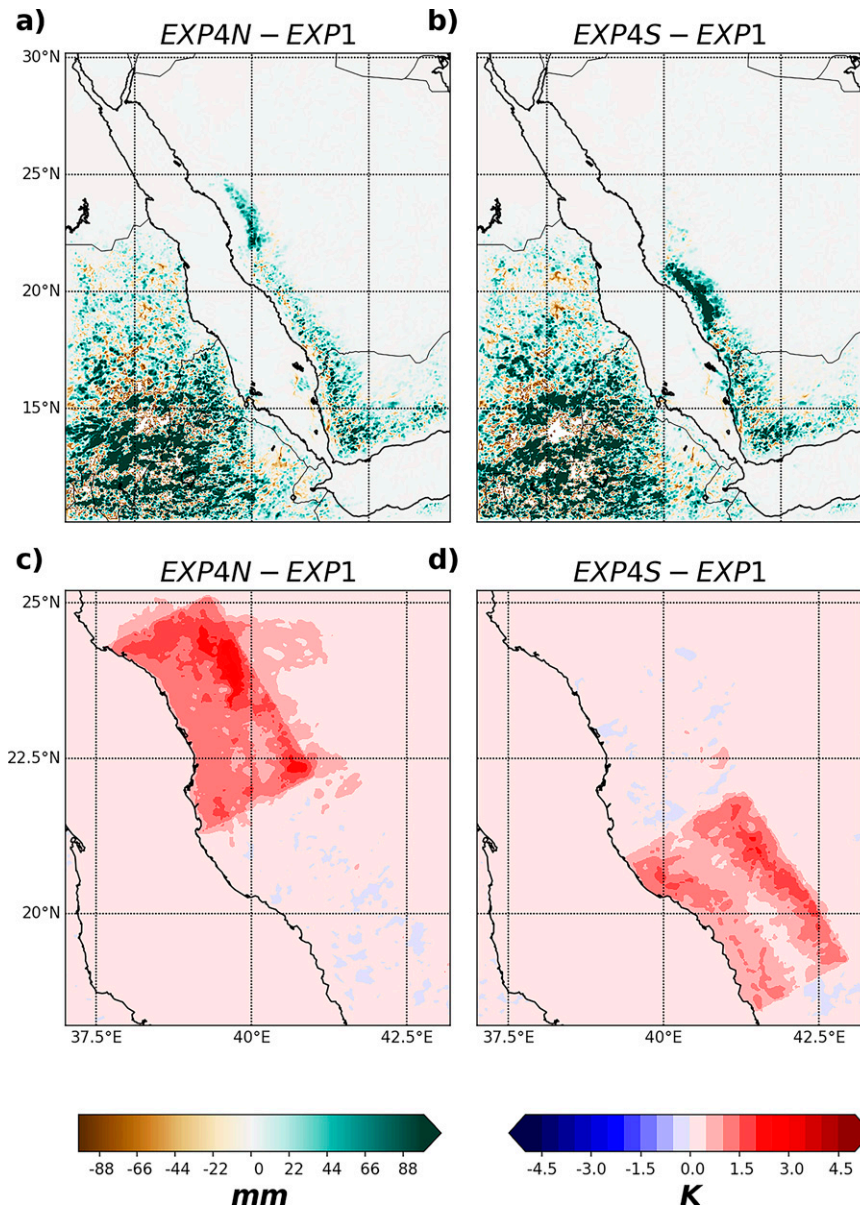
FIG. 12. Change with respect to the control EXP1 in accumulated (July–September 2013) precipitation (mm) for (a) EXP4N − EXP1 and (b) EXP4S − EXP1, and surface air temperature (K) for (c) EXP4N − EXP1 and (d) EXP4S − EXP1.

(Fig. 7a). In EXP4 we see an approximately 20% increase in relative humidity at a height of 4.5 km in comparison with the reference experiment (Fig. 11f). EXP4 demonstrates the increase in accumulated precipitation up to 250 mm in comparison with the control run (Fig. 8c). Thus, decreasing the surface albedo to 0.08 leads to a fourfold increase in both precipitation and evaporation compared with the reference experiment (Fig. 9). About 3.4 Gt of accumulated water $\Delta(P - E)$ is generated for three months in our simulations.

The surface albedo in EXP4 corresponds to the albedo of ocean. It is low and would be difficult to achieve. Therefore we

conduct the more realistic EXP5, where surface albedo is assumed to be 0.2, mimicking the albedo of solar panels installed in the large geoengineered area (Fig. 2). It is known that the reflection of solar radiation by solar panels could be reduced to 4% (Behera et al. 2020). However, about 15% of absorbed solar energy is converted to electricity, so effectively only 80% of solar flux goes to heat, which corresponds to the surface albedo of 0.2. We found that the surface modification in EXP5 leads to an increase in rainfall over the highlighted area (Figs. 8d and 9a). As expected, the added precipitation (1.5 Gt) is less than in EXP4, but still significant. Installing solar panels increases precipitation
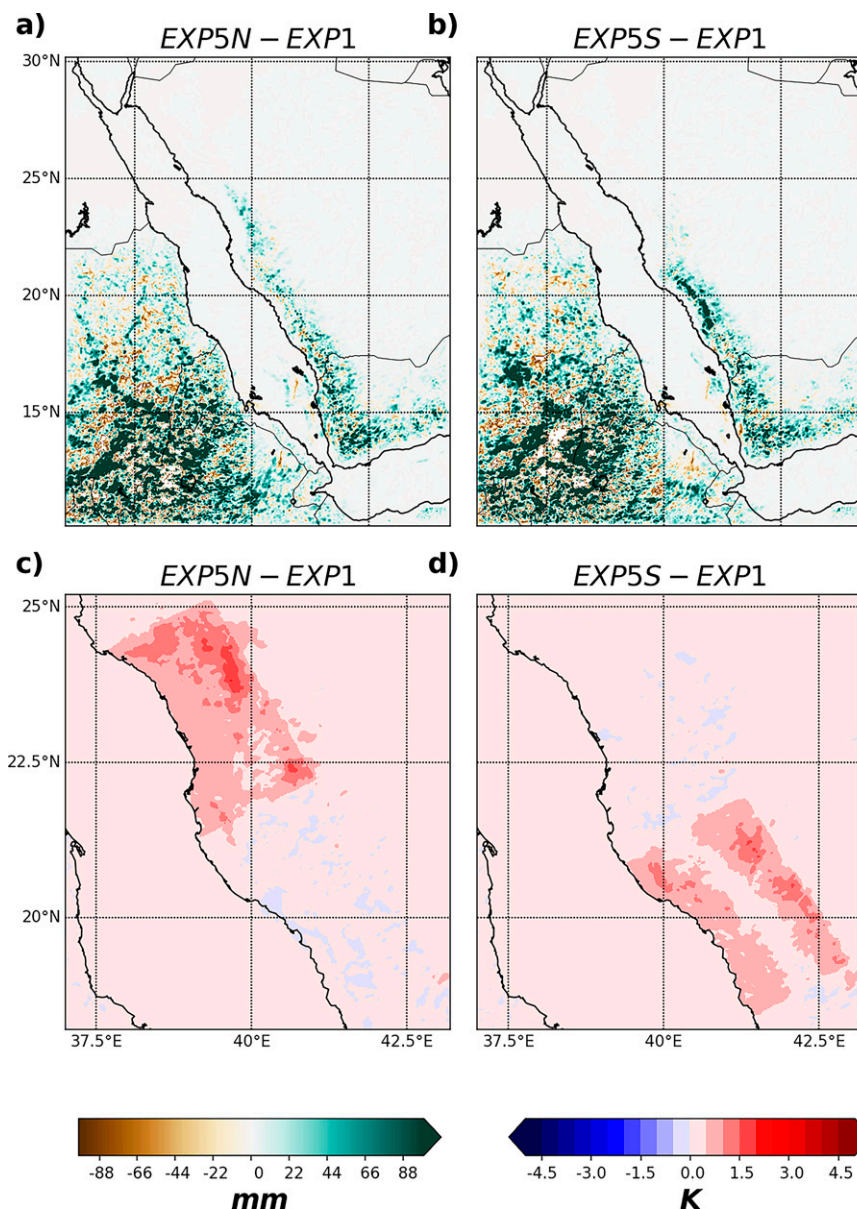
FIG. 13. Change with respect to control EXP1 in accumulated (July–September 2013) precipitation (mm) for (a) EXP5N − EXP1 and (b) EXP5S − EXP1, and surface air temperature (K) for (c) EXP5N − EXP1 and (d) EXP5S − EXP1.

and simultaneously provides an extra source of renewable energy that can be used for water desalination or other needs. The drawback is the increase of the near-surface air temperatures.

3) SENSITIVITY TO ROUGHNESS LENGTH

In addition to land-use type and surface albedo, which both play a significant role in PBL, surface roughness can also affect the energy exchange between land and atmosphere. Sud and Smith (1985) showed that rainfall over and adjacent to the Sahara Desert is sensitive to the roughness of the desert surface. A reduction of surface roughness from 0.45 m, which is about the average of all land, to 0.02 m, caused a significant change in global rainfall distribution over the land and nearby ocean regions (Sud et al. 1988).

In the EXP2, we chose a length associated with broadleaf forest, as suggested in the WRF land surface model (LSM). In the experiment EXP5, in order to isolate the surface albedo effect, we kept the default surface roughness length, which corresponds to the coastal semidesert. It varies from 0.009 m for bare land to 0.06 m for shrub land, with a 0.025-m average for the entire large geoengineered area.

To test the effect of roughness we conducted a sensitivity experiment (EXP5Z) that is similar to EXP5, but in addition to
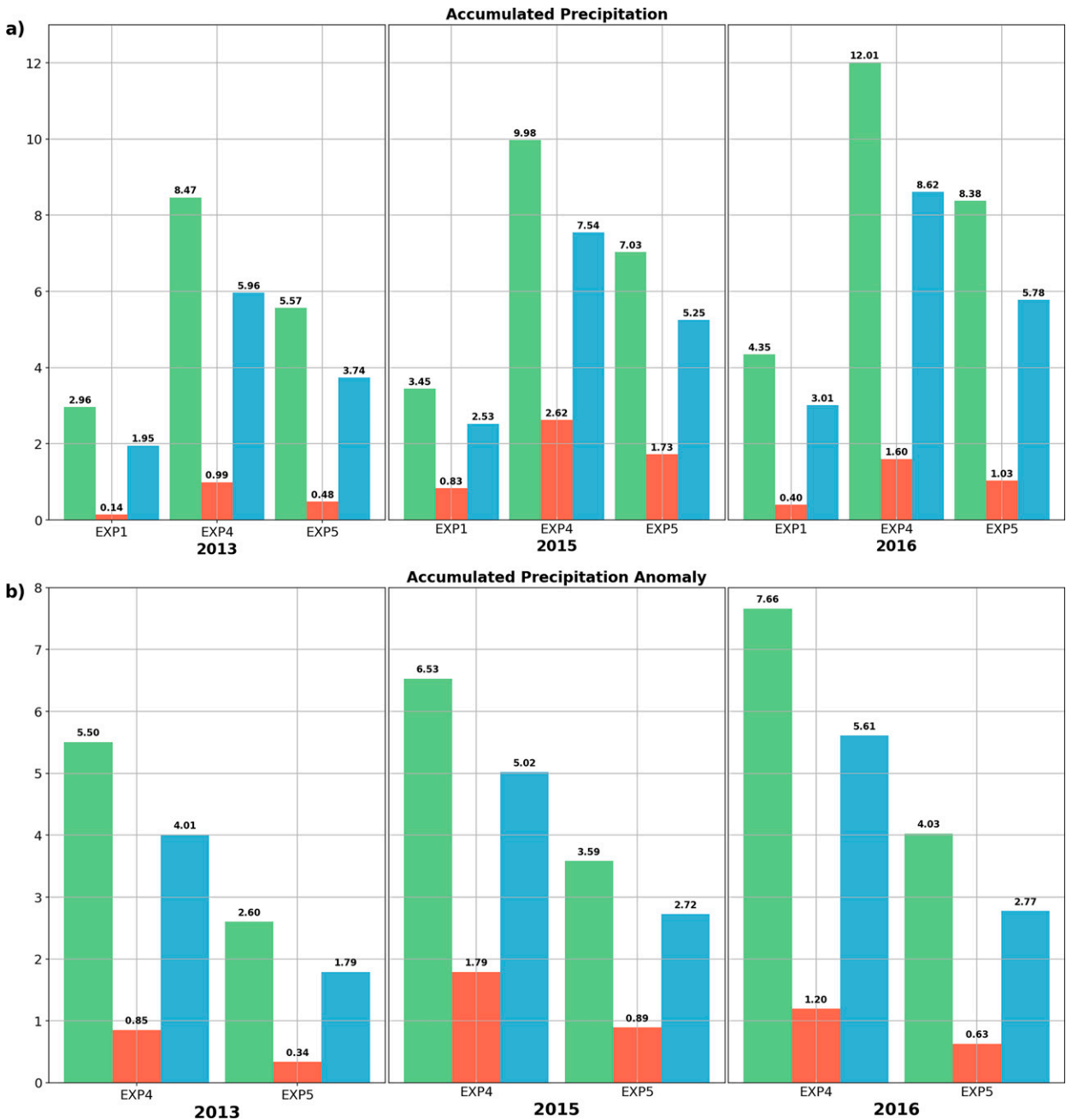
FIG. 14. (a) Accumulated (for July–September of 2013, 2015, 2016) precipitation *P* (Gt) over large (green), northern (red), and southern (blue) geoengineered areas in EXP1, EXP4, and EXP5. (b) Change of accumulated (July–September of 2013, 2015, 2016) precipitation Δ*P* (Gt) over large (green), northern (red), and southern (blue) geoengineering areas in EXP4, and EXP5 with respect to EXP1.

setting 0.2 surface albedo, we assume the surface roughness length in the entire large geoengineered area to be 0.06 m, which in turn assumes that shrubs cover all of the area. The mean roughness length in the geoengineered region in EXP5 is 0.025 m, so on average we increased the roughness length more than 2 times. We assume that the shrub land roughness is representative

for the near-surface panel installations. In our case, the increase of roughness caused small precipitation changes (Fig. 9b). We noticed a slight increase in rainfall compared with EXP5 in the northern highlighted region. Simultaneously, the precipitation in the southern area, where most of the surface is covered by shrubs and has a roughness of 0.06 m, decreased. Figure 9f shows that
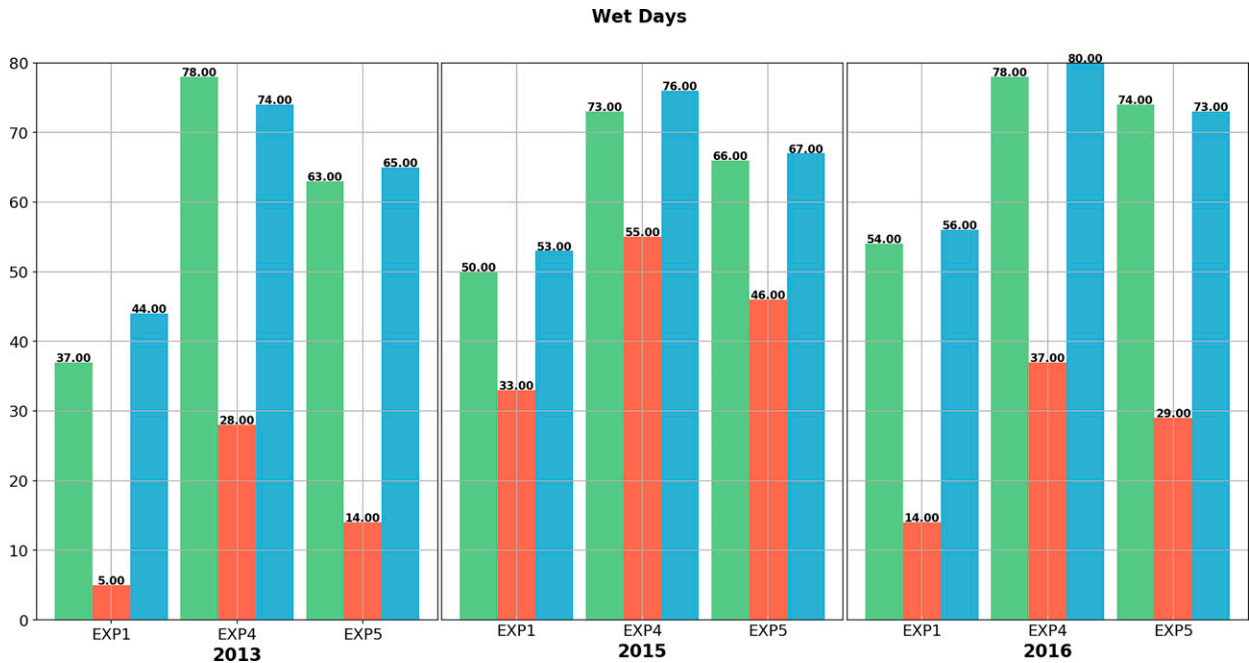
**Wet Days**



Fig. 15. Number of wet days $[(1/N)\sum_{i=1}^{N} P_i > 0.2$ mm$]$ in EXP1, EXP4, and EXP5 for July–September of 2013, 2015, and 2016.

$\Delta(P - E)$ in both EXP5 and EXP5Z is quite close. We therefore conclude that in our case surface roughness in not a leading physical mechanism affecting precipitation over the RS coastal plain.

### 4) Sensitivity to size, geographic location, and background topography of the geoengineered areas

To investigate the influence of the background topography and location of the geoengineering area on breeze circulation and consequently on the amount of added precipitation, we conducted four additional experiments (EXP4N, EXP4S and EXP5N, EXP5S). In experiments EXP4N and EXP4S we applied the same surface modification as in EXP4, separately in the northern subarea where mountain range height is about 1 km, and in the southern subarea (Fig. 2b), where the land elevation is twice as high. Similarly, in experiments EXP5N and EXP5S we applied the same surface albedo modification as in EXP5, but in only one of the subareas. Figures 12 and 13 show the changes in accumulated precipitation and surface air temperature with respect to the control run in all subarea experiments. All experiments demonstrate an increase in precipitation (Figs. 12a and 13a) and surface temperature (Figs. 12c and 13c). The southern subarea generates much more added rainwater $\Delta(P - E)$ than the northern one. The total added accumulated water in EXP4S is 1.6 Gt, and in EXP5S is 0.7 Gt (Fig. 9). The geoengineered area warms up to 2 K in EXP4N, EXP4S, and up to 1 K in EXP5N, EXP5S (Figs. 12d and 13d).

In Fig. 9 we compare the area-integrated cumulative precipitation in all albedo experiments. This demonstrates that the albedo modifications in EXP5 and EXP4S generate 1.5–1.6 Gt of added water. This is twice the annual amount of

rainwater currently collected and stored in Saudi Arabia. In all albedo experiments, the northern region is much less productive in terms of added precipitation than the southern region. This is because the breeze intensity and the terrain effect are weaker in the northern region than in the southern region. This suggests that installing solar panels in the southern geoengineered area could be a more efficient option than geoengineering the northern area or the entire large area.

To test the robustness of our results we repeated the albedo experiments (EXP4 and EXP5) for the summers of 2015 and 2016 (Figs. 14 and 15 ). We found that 2013, the year chosen for the analysis, had fewer wet days (defined as days with averaged daily precipitation higher than 0.2 mm) and less precipitation than in 2015 and 2016. Thus, we have probably underestimated the added water effect based on the analysis for 2013 by about 10%. However, all of the conclusions from our 2013 analysis remain the same for the 2015 and 2016 simulations (Figs. 14 and 15).

### 5. Conclusions

In this study we evaluate the effects of regional-scale modifications of land surface characteristics on coastal precipitation, aiming at developing a regular and reliable source of freshwater that could be collected, effectively stored, and reused. We performed a series of numerical experiments using the cloud-resolving WRF Model, altering the surface properties over the $150 \times 10^3$ km$^2$ coastal area by converting bare land into a wide-leaf forest, altering soil moisture, changing surface roughness length, and/or varying surface albedo.

We found that afforestation, soil watering, and increasing of surface albedo cool the region by about 2 K, but decrease

precipitation in the breeze affected areas. This is because land-cooling damps sea breeze circulation and decreases water vapor flux from sea to land. Conversely, a decrease of surface albedo warms the coastal regions by about 1–2 K, strengthens the sea breezes, and increases precipitation. The precipitation response is sensitive to the geopositioning and size of the geoengineered area. The more robust increase in rainfall and added water is found in the southern part of the geoengineered area, where mountains are higher and sea breezes are stronger. Imposing an 0.08 albedo gives the most substantial effect on generated water (3.3 Gt in EXP4). Still, a more realistic albedo of 0.2 which mimics the large-scale installation of solar panel plants also gives a sizable increase of about 10 Mt of added water per square kilometer during the dry summer season (1.5 Gt in EXP5 and 0.7 Gt in EXP5S, see Table 2 for the experiment descriptions). The surface albedo geoengineering works best in the southern area in EXP4S and EXP5S, where the more intensive breeze and the stronger vertical instability in the boundary layer due to more vigorous surface heating combine to increase precipitation over the mountain slopes, where the orographic lift adds in triggering rainfall. The number of wet days in EXP4 and EXP5 almost doubles in comparison with EXP1.

Thus, our experiments show that changes in land surface characteristics modulate local breeze intensity and precipitation in the RS coastal plains and mountain slopes. The reduction of land albedo could most effectively be achieved by distributing solar panels over the near-coast mountains' slopes. Installing solar panels only in the southern region can generate 0.7 Gt of freshwater per summer season. Assuming that the annual per capita freshwater consumption in Saudi Arabia is 282 t (Ouda 2013), this amount of water could effectively cover the seasonal consumption of 2.5 million people. A diverse system of 449 water collecting reservoirs already exists at the Arabian Red Sea Coastal Plain. The deployment of solar panels is an attractive idea, as it facilitates the extraction of renewable energy resources. Assuming 15% efficiency of solar energy conversion to electricity, solar panels can effectively generate 50 W m$^{-2}$ of electricity on a daily average basis (Parida et al. 2011). The southern geoengineered region alone, with an area of $69 \times 10^3$ km$^2$, can generate 3.45 TW of clean energy (Castellano 2010) free from greenhouse emissions. While our experiments are idealized, they point to the feasibility of freshwater recovery from sea breezes by regional land surface geoengineering. Further research, including field experiments, should be conducted to assess the efficacy of the proposed measures. Because our methods utilize sea breeze circulation, which is a local process that drives evaporated moisture from the RS to the land, the probability of adverse climatic effects to surrounding regions is low. Local-scale sea breeze management could be an attractive and viable adaptation measure to increasing water scarcity in the arid Arabian Peninsula in the course of ongoing climate change.

In light of the Saudi and Middle East Green Initiative, that assumes large-scale afforestation in the desert areas, this study develops a scientific approach for optimizing spatial distribution of tree planting areas and evaluating their local climate impacts. For example, our study shows that afforestation of the Red Sea

coastal plain would not be beneficial in terms of increasing precipitation over the Arabian Red Sea coastal plain.

In the twenty-first century, environmental changes will have significant societal impacts that require a thorough planning of adaptation and mitigation measures. The Arabian Peninsula and the Middle East are especially vulnerable to climate change, as they already have harsh climates. Therefore, designing nature-based regional-scale geoengineering adaptation solutions and developing region-specific modeling technologies to counteract global warming is paramount.

*Data availability statement.* The MERRA-2 reanalysis is available at https://gmao.gsfc.nasa.gov/reanalysis/MERRA2/. The ECMWF Operational Analysis (ECMWF-OA) data are restricted and were retrieved from http://apps.ecmwf.int/archivecatalogue/?type=4v&class=od&stream=oper&expver=1 (with a membership). The TRMM daily accumulated precipitation is available at http://disc.sci.gsfc.nasa.gov/precipitation/documentation/TRMM_README/TRMM_3B42_readm. Copies of the input datasets and details of the WRF Model configuration can be downloaded from the KAUST repository (http://hdl.handle.net/10754/664899) or by email request to suleiman.mostamandi@kaust.edu.sa.

### REFERENCES

Abdullah, M., and M. Al-Mazroui, 1998: Climatological study of the southwestern region of Saudi Arabia. I. Rainfall analysis. *Climate Res.*, **9**, 213–223, https://doi.org/10.3354/cr009213.

Ahmed, F. E., R. Hashaikeh, and N. Hilal, 2019: Solar powered desalination–technology, energy and future outlook. *Desalination*, **453**, 54–76, https://doi.org/10.1016/j.desal.2018.12.002.

Al-Jerash, M. A., 1985: Climatic subdivisions in Saudi Arabia: An application of principal component analysis. *J. Climate*, **5**, 307–323, https://doi.org/10.1002/joc.3370050307.

Almazroui, M., M. Nazrul Islam, H. Athar, P. Jones, and M. A. Rahman, 2012: Recent climate change in the Arabian Peninsula: Annual rainfall and temperature analysis of Saudi Arabia for 1978–2009. *Int. J. Climatol.*, **32**, 953–966, https://doi.org/10.1002/joc.3446.

Al-Rashed, M. F., and M. M. Sherif, 2000: Water resources in the GCC countries: An overview. *Water Resour. Manage.*, **14**, 59–75, https://doi.org/10.1023/A:1008127027743.

Al-Taher, A. A., 1994: Drought and human adjustment in Saudi Arabia. *GeoJournal*, **33**, 411–422, https://doi.org/10.1007/BF00806424.

Al-Zahrani, K. H., and E. Elhag, 2003: *Agricultural Development during the Era of King Fahd.* King Saud University, 48–56.

——, and Coauthors, 2011: Water in the kingdom of Saudi Arabia: Sustainable management options. *J. Anim. Plant Sci.*, **21**, 601–604.

Awad, A. M., and M. Almazroui, 2016: Climatology of the winter red sea trough. *Atmos. Res.*, **182**, 20–29, https://doi.org/10.1016/j.atmosres.2016.07.019.

Baklanov, A., U. Korsholm, A. Mahura, C. Petersen, and A. Gross, 2008: ENVIRO-HIRLAM: On-line coupled modelling of urban meteorology and air pollution. *Adv. Sci. Res.*, **2**, 41–46, https://doi.org/10.5194/asr-2-41-2008.

Behera, S., P. W. Fry, H. Francis, C.-Y. Jin, and M. Hopkinson, 2020: Broadband, wide-angle antireflection in GaAs through surface nano-structuring for solar cell applications. *Sci. Rep.*, **10**, 6269, https://doi.org/10.1038/s41598-020-63327-7.

Bonelle, J., Y. Fournier, and C. Moulinec, 2018: New polyhedral discretisation methods applied to the Richards equation: CDO schemes in code_saturne. *Comput. Fluids*, **173**, 93–102, https://doi.org/10.1016/j.compfluid.2018.03.026.

Bright, R. M., K. Zhao, R. B. Jackson, and F. Cherubini, 2015: Quantifying surface albedo and other direct biogeophysical climate forcings of forestry activities. *Global Change Biol.*, **21**, 3246–3266, https://doi.org/10.1111/gcb.12951.

Brown, B., 1935: Conformal and equiareal world maps. *Amer. Math. Mon.*, **42**, 212–223, https://doi.org/10.1080/00029890.1935.11987707.

Buchard, V., and Coauthors, 2017: The MERRA-2 aerosol reanalysis, 1980 onward. Part II: Evaluation and case studies. *J. Climate*, **30**, 6851–6872, https://doi.org/10.1175/JCLI-D-16-0613.1.

Cao, Q., D. Yu, M. Georgescu, Z. Han, and J. Wu, 2015: Impacts of land use and land cover change on regional climate: A case study in the agro-pastoral transitional zone of China. *Environ. Res. Lett.*, **10**, 124025, https://doi.org/10.1088/1748-9326/10/12/124025.

Castellano, N. R., 2010: *Solar Panel Processing*. Old City Publishing, 92 pp.

Chaidez, V., D. Dreano, S. Agusti, C. M. Duarte, and I. Hoteit, 2017: Decadal trends in red sea maximum surface temperature. *Sci. Rep.*, **7**, 8144, https://doi.org/10.1038/s41598-017-08146-z.

Chen, F., and R. Avissar, 1994a: Impact of land-surface moisture variability on local shallow convective cumulus and precipitation in large-scale models. *J. Appl. Meteor. Climatol.*, **33**, 1382–1401, https://doi.org/10.1175/1520-0450(1994)033<1382:IOLSMV>2.0.CO;2.

——, and ——, 1994b: The impact of land-surface wetness heterogeneity on mesoscale heat fluxes. *J. Appl. Meteor. Climatol.*, **33**, 1323–1340, https://doi.org/10.1175/1520-0450(1994)033<1323:TIOLSW>2.0.CO;2.

Climatestotravel.com, 2021: Climate – Saudi Arabia. https://www.climatestotravel.com/climate/saudi-arabia.

Crutzen, P. J., 2006: Albedo enhancement by stratospheric sulfur injections: A contribution to resolve a policy dilemma? *Climatic Change*, **77**, 211, https://doi.org/10.1007/s10584-006-9101-y.

Davidson, A., and A. McKerrow, 2016: GAP/LANDFIRE national terrestrial ecosystems 2011. U.S. Geological Survey, accessed 11 November 2020, https://doi.org/10.5066/F7ZS2TM0.

Davis, S. R., J. T. Farrar, R. A. Weller, H. Jiang, and L. J. Pratt, 2019: The land-sea breeze of the red sea: Observations, simulations, and relationships to regional moisture transport. *J. Geophys. Res. Atmos.*, **124**, 13 803–13 825, https://doi.org/10.1029/2019JD031007.

De Meij, A., and J. Vinuesa, 2014: Impact of SRTM and Corine Land Cover data on meteorological parameters using WRF. *Atmos. Res.*, **143**, 351–370, https://doi.org/10.1016/j.atmosres.2014.03.004.

De Vries, A. J., E. Tyrlis, D. Edry, S. Krichak, B. Steil, and J. Lelieveld, 2013: Extreme precipitation events in the Middle East: Dynamics of the active red sea trough. *J. Geophys. Res. Atmos.*, **118**, 7087–7108, https://doi.org/10.1002/jgrd.50569.

——, H. G. Ouwersloot, S. B. Feldstein, M. Riemer, A. M. El Kenawy, M. F. McCabe, and J. Lelieveld, 2018: Identification of tropical-extratropical interactions and extreme precipitation events in the Middle East based on potential vorticity and moisture transport. *J. Geophys. Res. Atmos.*, **123**, 861–881, https://doi.org/10.1002/2017JD027587.

Dogar, M. M., G. Stenchikov, S. Osipov, B. Wyman, and M. Zhao, 2017: Sensitivity of the regional climate in the Middle East and North Africa to volcanic perturbations. *J. Geophys. Res. Atmos.*, **122**, 7922–7948, https://doi.org/10.1002/2017JD026783.

Drobinski, P., S. Bastin, A. Dabas, P. Delville, and O. Reitebuch, 2006: Variability of three-dimensional sea breeze structure in southern France: Observations and evaluation of empirical scaling laws. *Ann. Geophys.*, **24**, 1783–1799, https://doi.org/10.5194/angeo-24-1783-2006.

ECMWF, 2016: IFS Documentation CY41R2: Part I: Observations. ECMWF, 72 pp., https://doi.org/10.21957/9phrx9eu.

El Kenawy, A. M., M. F. McCabe, G. L. Stenchikov, and J. Raj, 2014: Multi-decadal classification of synoptic weather types, observed trends and links to rainfall characteristics over Saudi Arabia. *Front. Environ. Sci.*, **2**, 37, https://doi.org/10.3389/fenvs.2014.00037.

Eltahir, E. A., 1989: A feedback mechanism in annual rainfall, Central Sudan. *J. Hydrol.*, **110**, 323–334, https://doi.org/10.1016/0022-1694(89)90195-9.

——, and R. L. Bras, 1996: Precipitation recycling. *Rev. Geophys.*, **34**, 367–378, https://doi.org/10.1029/96RG01927.

Evans, J. P., and S. Westra, 2012: Investigating the mechanisms of diurnal rainfall variability using a regional climate model. *J. Climate*, **25**, 7232–7247, https://doi.org/10.1175/JCLI-D-11-00616.1.

Feddema, J. J., K. W. Oleson, G. B. Bonan, L. O. Mearns, L. E. Buja, G. A. Meehl, and W. M. Washington, 2005: The importance of land-cover change in simulating future climates. *Science*, **310**, 1674–1678, https://doi.org/10.1126/science.1118160.

Fitz, D. R., and K. Bumiller, 2000: Evaluation of watering to control dust in high winds. *J. Air Waste Manage. Assoc.*, **50**, 570–577, https://doi.org/10.1080/10473289.2000.10464037.

Foley, J., and Coauthors, 2005: Global consequences of land use. *Science*, **309**, 570–574, https://doi.org/10.1126/science.1111772.

Fox, T. A., and L. Chapman, 2011: Engineering geo-engineering. *Meteor. Appl.*, **18**, 1–8, https://doi.org/10.1002/met.245.

Hameed, M., H. Moradkhani, A. Ahmadalipour, H. Moftakhari, P. Abbaszadeh, and A. Alipour, 2019: A review of the 21st century challenges in the food-energy-water security in the Middle East. *Water*, **11**, 682, https://doi.org/10.3390/w11040682.

Hasanean, H., and M. Almazroui, 2015: Rainfall: Features and variations over Saudi Arabia, a review. *Climate*, **3**, 578–626, https://doi.org/10.3390/cli3030578.

Haurwitz, B., 1947: Comments on the sea-breeze circulation. *J. Meteor.*, **4**, 1–8, https://doi.org/10.1175/1520-0469(1947)004<0001:COTSBC>2.0.CO;2.

Haywood, J. M., A. Jones, N. Bellouin, and D. Stephenson, 2013: Asymmetric forcing from stratospheric aerosols impacts Sahelian rainfall. *Nat. Climate Change*, **3**, 660–665, https://doi.org/10.1038/nclimate1857.

Hill, C., P. Fitzpatrick, J. Corbin, and Y. Lau, 2010: Summertime precipitation regimes associated with the sea breeze and land

breeze in southern Mississippi and eastern Louisiana. *Wea. Forecasting*, **25**, 1755–1779, https://doi.org/10.1175/2010WAF 2222340.1.

Huffman, G. J., and Coauthors, 2007: The TRMM Multisatellite Precipitation Analysis (TMPA): Quasi-global, multiyear, combined-sensor precipitation estimates at fine scales. *J. Hydrometeor.*, **8**, 38–55, https://doi.org/10.1175/JHM560.1.

Iacono, M. J., J. S. Delamere, E. J. Mlawer, M. W. Shephard, S. A. Clough, and W. D. Collins, 2008: Radiative forcing by long-lived greenhouse gases: Calculations with the AER radiative transfer models. *J. Geophys. Res.*, **113**, D13103, https://doi.org/10.1029/2008JD009944.

Ismail, A., M. H. A. Samad, and A. M. A. Rahman, 2011: The investigation of green roof and white roof cooling potential on single storey residential building in the Malaysian climate. *World Acad. Sci. Eng. Technol.*, **76**, 129–137.

Janjić, Z. I., 1994: The step-mountain eta coordinate model: Further developments of the convection, viscous sublayer, and turbulence closure schemes. *Mon. Wea. Rev.*, **122**, 927–945, https://doi.org/10.1175/1520-0493(1994)122<0927:TSMECM>2.0.CO;2.

Junkermann, W., J. Hacker, T. Lyons, and U. Nair, 2009: Land use change suppresses precipitation. *Atmos. Chem. Phys.*, **9**, 6531–6539, https://doi.org/10.5194/acp-9-6531-2009.

Khan, B., Y. Abualnaja, A. M. Al-Subhi, M. Nellayaputhenpeedika, M. Nellikkattu Thody, and A. P. Sturman, 2018: Climatology of sea breezes along the red sea coast of Saudi Arabia. *Int. J. Climatol.*, **38**, 3633–3650, https://doi.org/10.1002/joc.5523.

Köppen, W., 1936: *Das geographische System der Klimate.* Vol. 1, *Handbuch der Klimatologie*, W. Köppen and G. Geiger, Eds., Gebrüder Borntraeger, 44 pp.

Krenke, A., G. Stenchikov, and D. Turkov, 1991: The use of a hydrodynamic model for assessing the role of land surface in climatic changes. *Izv. Akad. Nauk SSSR, Ser. Geofiz.*, **5**, 23–34.

Kucera, P., and Coauthors, 2010: Features of the weather modification assessment project in the southwest region of Saudi Arabia. *J. Wea. Modif.*, **42**, 78–103.

Kunstmann, H., and G. Jung, 2007: Influence of soil-moisture and land use change on precipitation in the Volta basin of West Africa. *Int. J. River Basin Manage.*, **5**, 9–16, https://doi.org/10.1080/15715124.2007.9635301.

Li, Y., E. Kalnay, S. Motesharrei, J. Rivas, F. Kucharski, D. Kirk-Davidoff, E. Bach, and N. Zeng, 2018: Climate model shows large-scale wind and solar farms in the Sahara increase rain and vegetation. *Science*, **361**, 1019–1022, https://doi.org/10.1126/science.aar5629.

Liu, Z., D. Ostrenga, W. Teng, and S. Kempler, 2012: Tropical Rainfall Measuring Mission (TRMM) precipitation data and services for research and applications. *Bull. Amer. Meteor. Soc.*, **93**, 1317–1325, https://doi.org/10.1175/BAMS-D-11-00152.1.

Lopez, O., G. Stenchikov, and T. M. Missimer, 2014: Water management during climate change using aquifer storage and recovery of stormwater in a dunefield in western Saudi Arabia. *Environ. Res. Lett.*, **9**, 075008, https://doi.org/10.1088/1748-9326/9/7/075008.

Mapes, B. E., T. T. Warner, and X. Mei, 2003: Diurnal patterns of rainfall in northwestern South America. Part III: Diurnal gravity waves and nocturnal convection offshore. *Mon. Wea. Rev.*, **131**, 830–844, https://doi.org/10.1175/1520-0493(2003)131<0830:DPORIN>2.0.CO;2.

Mazroui, A. A., and S. Farrah, 2017: The UAE seeks leading position in global rain enhancement research. *J. Wea. Modif.*, **49**, 54–59.

Mesinger, F., and A. Arakawa, 1976: Numerical methods used in atmospheric models. GARP Publ. 17, 70 pp., https://core.ac.uk/download/pdf/141499575.pdf.

Miguez-Macho, G., G. L. Stenchikov, and A. Robock, 2004: Spectral nudging to eliminate the effects of domain position and geometry in regional climate model simulations. *J. Geophys. Res.*, **109**, D13104, https://doi.org/10.1029/2003JD004495.

Miller, S., B. Keim, R. Talbot, and H. Mao, 2003: Sea breeze: Structure, forecasting, and impacts. *Rev. Geophys.*, **41**, 1011, https://doi.org/10.1029/2003RG000124.

Ministry of Environment Water and Agriculture, 2017: Annual report. Riyadh, Saudi Arabia, https://www.mewa.gov.sa/en/Pages/default.aspx.

Morcos, S. A., 1970: Physical and chemical oceanography of the Red Sea. *Oceanogr. Mar. Biol. Annu. Rev.*, **8**, 73–202.

Nassir, S. A., 2012: Annual and seasonal mean net evaporation rates of the Red Sea water during Jan 1958-Dec 2007. M.S. thesis, Science in Physical Oceanography, University of Bergen, 46 pp.

Ouda, O. K., 2013: Towards assessment of Saudi Arabia public awareness of water shortage problem. *Resour. Environ.*, **3**, 10–13, https://doi.org/10.5923/j.re.20130301.02.

Papanastasiou, D., and D. Melas, 2009: Climatology and impact on air quality of sea breeze in an urban coastal environment. *Int. J. Climatol.*, **29**, 305–315, https://doi.org/10.1002/joc.1707.

Parajuli, S. P., G. L. Stenchikov, A. Ukhov, I. Shevchenko, O. Dubovik, and A. Lopatin, 2020: Aerosol vertical distribution and interactions with land/sea breezes over the eastern coast of the Red Sea from lidar data and high-resolution WRF-Chem simulations. *Atmos. Chem. Phys.*, **20**, 16089–16116, https://doi.org/10.5194/acp-20-16089-2020.

Parida, B., S. Iniyan, and R. Goic, 2011: A review of solar photovoltaic technologies. *Renew. Sustain. Energy Rev.*, **15**, 1625–1636, https://doi.org/10.1016/j.rser.2010.11.032.

Pedgley, D., 1974: An outline of the weather and climate of the Red Sea. *L'Oceanographie Physique de la Mer Rouge: Symp. de l'Association International des Sciences Physiques de l'Océan*, Paris, France, UNESCO, 9–27.

Pielke, R. A., Sr., 2001: Influence of the spatial distribution of vegetation and soils on the prediction of cumulus convective rainfall. *Rev. Geophys.*, **39**, 151–177, https://doi.org/10.1029/1999RG000072.

——, J. Adegoke, A. BeltraaN-Przekurat, C. A. Hiemstra, J. Lin, U. S. Nair, D. Niyogi, and T. E. Nobis, 2007: An overview of regional land-use and land-cover impacts on rainfall. *Tellus*, **59B**, 587–601, https://doi.org/10.1111/j.1600-0889.2007.00251.x.

Pitman, A., 2003: The evolution of, and revolution in, land surface schemes designed for climate models. *Int. J. Climatol.*, **23**, 479–510, https://doi.org/10.1002/joc.893.

Pokhrel, R., and H. Lee, 2011: Estimation of the effective zone of sea/land breeze in a coastal area. *Atmos. Pollut. Res.*, **2**, 106–115, https://doi.org/10.5094/APR.2011.013.

Pongratz, J., D. B. Lobell, L. Cao, and K. Caldeira, 2012: Crop yields in a geoengineered climate. *Nat. Climate Change*, **2**, 101–105, https://doi.org/10.1038/nclimate1373.

Qian, J., 2008: Why precipitation is mostly concentrated over islands in the maritime continent. *J. Atmos. Sci.*, **65**, 1428–1441, https://doi.org/10.1175/2007JAS2422.1.

Qian, T., C. C. Epifanio, and F. Zhang, 2012: Topographic effects on the tropical land and sea breeze. *J. Atmos. Sci.*, **69**, 130–149, https://doi.org/10.1175/JAS-D-11-011.1.

Ralston, D. K., H. Jiang, and J. T. Farrar, 2013: Waves in the red sea: Response to monsoonal and mountain gap winds. *Cont. Shelf Res.*, **65**, 1–13, https://doi.org/10.1016/j.csr.2013.05.017.

Randles, C., and Coauthors, 2017: The MERRA-2 aerosol reanalysis, 1980 onward. Part I: System description and data assimilation evaluation. *J. Climate*, **30**, 6823–6850, https://doi.org/10.1175/JCLI-D-16-0609.1.

Rasul, N. M., and I. C. Stewart, 2015: *The Red Sea: The Formation, Morphology, Oceanography and Environment of a Young Ocean Basin.* Springer, 647 pp.

Robock, A., L. Oman, and G. L. Stenchikov, 2008: Regional climate responses to geoengineering with tropical and Arctic $SO_2$ injections. *J. Geophys. Res.*, **113**, D16101, https://doi.org/10.1029/2008JD010050.

Rodell, M., J. Famiglietti, D. Wiese, J. Reager, H. Beaudoing, F. W. Landerer, and M.-H. Lo, 2018: Emerging trends in global freshwater availability. *Nature*, **557**, 651–659, https://doi.org/10.1038/s41586-018-0123-1.

*Saudi Gazette*, 2016: Kingdom's groundwater "will run out in 13 years." *Saudi Gazette*, 9 February, http://saudigazette.com.sa/article/148336.

Sertel, E., A. Robock, and C. Ormeci, 2010: Impacts of land cover data quality on regional climate simulations. *Int. J. Climatol.*, **30**, 1942–1953, https://doi.org/10.1002/joc.2036.

Shepherd, J. G., 2009: Geoengineering the climate: Science, governance and uncertainty. The Royal Society, 82 pp., https://royalsociety.org/topics-policy/publications/2009/geoengineering-climate/.

Shrestha, R. K., and R. Lal, 2006: Ecosystem carbon budgeting and soil carbon sequestration in reclaimed mine soil. *Environ. Int.*, **32**, 781–796, https://doi.org/10.1016/j.envint.2006.05.001.

Sinha, R. K., 2004: *Modern Plant Physiology.* CRC Press, 620 pp.

Skamarock, W. C., J. B. Klemp, J. Dudhia, D. O. Gill, D. M. Barker, W. Wang, and J. G. Powers, 2005: A description of the Advanced Research WRF version 2. *NCAR Tech. Note* NCAR/TN-468+STR, 88 pp., https://doi.org/10.5065/D6DZ069T.

Snyder, J. P., 1978: Equidistant conic map projections. *Ann. Assoc. Amer. Geogr.*, **68**, 373–383, https://doi.org/10.1111/j.1467-8306.1978.tb01201.x.

Sofianos, S. S., and W. E. Johns, 2002: An oceanic General Circulation Model (OGCM) investigation of the Red Sea circulation, 1. Exchange between the Red Sea and the Indian Ocean. *J. Geophys. Res.*, **107**, 3196, https://doi.org/10.1029/2001JC001184.

Steyn, D., and D. Faulkner, 1986: The climatology of sea-breezes in the lower Fraser Valley, B.C. *Climatol. Bull.*, **20**, 21–39.

Sud, Y., and W. Smith, 1985: The influence of surface roughness of deserts on the July circulation. *Bound.-Layer Meteor.*, **33**, 15–49, https://doi.org/10.1007/BF00137034.

——, J. Shukla, and Y. Mintz, 1988: Influence of land surface roughness on atmospheric circulation and precipitation: A sensitivity study with a general circulation model. *J. Appl. Meteor. Climatol.*, **27**, 1036–1054, https://doi.org/10.1175/1520-0450(1988)027<1036:IOLSRO>2.0.CO;2.

Swann, A. L., I. Y. Fung, and J. C. Chiang, 2012: Mid-latitude afforestation shifts general circulation and tropical precipitation. *Proc. Natl. Acad. Sci. USA*, **109**, 712–716, https://doi.org/10.1073/pnas.1116706108.

Tanarhte, M., P. Hadjinicolaou, and J. Lelieveld, 2012: Intercomparison of temperature and precipitation data sets based on observations in the Mediterranean and the Middle East. *J. Geophys. Res.*, **117**, D12102, https://doi.org/10.1029/2011JD017293.

Tarawneh, Q. Y., and S. Chowdhury, 2018: Trends of climate change in Saudi Arabia: Implications on water resources. *Climate*, **6**, 8, https://doi.org/10.3390/cli6010008.

Ter Maat, H., R. Hutjes, R. Ohba, H. Ueda, B. Bisselink, and T. Bauer, 2006: Meteorological impact assessment of possible large scale irrigation in southwest Saudi Arabia. *Global Planet. Change*, **54**, 183–201, https://doi.org/10.1016/j.gloplacha.2006.01.018.

Tewari, M., and Coauthors, 2004: Implementation and verification of the unified Noah land surface model in the WRF model. *20th Conf. on Weather Analysis and Forecasting/16th Conf. on Numerical Weather Prediction*, Seattle, WA, Amer. Meteor. Soc., 14.2a, https://ams.confex.com/ams/84Annual/techprogram/paper_69061.htm.

Thompson, G., P. R. Field, R. M. Rasmussen, and W. D. Hall, 2008: Explicit forecasts of winter precipitation using an improved bulk microphysics scheme. Part II: Implementation of a new snow parameterization. *Mon. Wea. Rev.*, **136**, 5095–5115, https://doi.org/10.1175/2008MWR2387.1.

Trenberth, K. E., and L. Smith, 2005: The mass of the atmosphere: A constraint on global analyses. *J. Climate*, **18**, 864–875, https://doi.org/10.1175/JCLI-3299.1.

——, and A. Dai, 2007: Effects of Mount Pinatubo volcanic eruption on the hydrological cycle as an analog of geoengineering. *Geophys. Res. Lett.*, **34**, L15702, https://doi.org/10.1029/2007GL030524.

Tsvieli, Y., and A. Zangvil, 2005: Synoptic climatological analysis of "wet" and "dry" red sea troughs over Israel. *Int. J. Climatol.*, **25**, 1997–2015, https://doi.org/10.1002/joc.1232.

Vitousek, P. M., H. A. Mooney, J. Lubchenco, and J. M. Melillo, 1997: Human domination of Earth's ecosystems. *Science*, **277**, 494–499, https://doi.org/10.1126/science.277.5325.494.

Zhu, L., Z. Meng, F. Zhang, and P. M. Markowski, 2017: The influence of sea-and land-breeze circulations on the diurnal variability in precipitation over a tropical island. *Atmos. Chem. Phys.*, **17**, 13 213–13 232, https://doi.org/10.5194/acp-17-13213-2017.

Zolina, O., A. Dufour, S. K. Gulev, and G. Stenchikov, 2017: Regional hydrological cycle over the red sea in ERA-Interim. *J. Hydrometeor.*, **18**, 65–83, https://doi.org/10.1175/JHM-D-16-0048.1.